PNAS RESEARCH ARTICLE | GENETICS OPEN ACCESS

Ectopic expression of meiotic cohesin generates chromosome instability in cancer cell line

Abdelhalim Boukaba[a], Jian Liu[a], Carl Ward[b], Qiongfang Wu[a], Alexei Arnaoutov[c], Jierong Liang[a], Elena M. Pugacheva[d], Mary Dasso[c], Victor Lobanenkov[d], Miguel Esteban[b], and Alexander V. Strunnikov[a,1]

Edited by Douglas Koshland, University of California, Berkeley, CA; received March 10, 2022; accepted August 23, 2022

Many tumors express meiotic genes that could potentially drive somatic chromosome instability. While germline cohesin subunits SMC1B, STAG3, and REC8 are widely expressed in many cancers, messenger RNA and protein for RAD21L subunit are expressed at very low levels. To elucidate the potential of meiotic cohesins to contribute to genome instability, their expression was investigated in human cell lines, predominately in DLD-1. While the induction of the REC8 complex resulted in a mild mitotic phenotype, the expression of the RAD21L complex produced an arrested but viable cell pool, thus providing a source of DNA damage, mitotic chromosome missegregation, sporadic polyteny, and altered gene expression. We also found that genomic binding profiles of ectopically expressed meiotic cohesin complexes were reminiscent of their corresponding specific binding patterns in testis. Furthermore, meiotic cohesins were found to localize to the same sites as BORIS/CTCFL, rather than CTCF sites normally associated with the somatic cohesin complex. These findings highlight the existence of a germline epigenomic memory that is conserved in cells that normally do not express meiotic genes. Our results reveal a mechanism of action by unduly expressed meiotic cohesins that potentially links them to aneuploidy and chromosomal mutations in affected cells.

chromosome instability | chromatin | centromere | cancer–testis genes | condensin

Significance

This work originated from mining of cancer genome data and proceeded to analyze the effects of ectopic expression of meiotic cohesins in mitotic cells in culture. In the process, apart from conclusively answering the question on mechanisms for RAD21L toxicity and its underrepresentation in tumor transcriptomes, we found an association of meiotic cohesin binding with BORIS/CTCFL sites in the normal testis. We also elucidated the patterns and outcomes of meiotic cohesin binding to chromosomes in model cell lines. Furthermore, we uncovered that RAD21L-based meiotic cohesin possesses a self-contained chromosome restructuring activity able to trigger sustainable but imperfect mitotic arrest leading to chromosomal instability. The discovered epigenomic and genetic mechanisms can be relevant to chromosome instability in cancer.

It is well established that a substantial number of malignant tumors express germline-specific genes (1–5). Among those, collectively named cancer–testis (CT) factors (6), there are some potent regulators of gene expression and/or chromatin structure. However, the role of such proteins in tumor biology is not well-studied and thus presently could be underestimated (7). Nevertheless, reports of functional dependence of cancer cells on activated CT genes are steadily accumulating (3, 8–14), suggesting that some CT genes could play roles in cancer onset rather than being merely "passengers" of tumor development. Furthermore, the somatic expression of germline chromatin proteins is conceptually similar to the epigenetic deregulation, with a novel epigenomic landscape generated not by a change of DNA or histone modification but by the emergence of unscheduled chromatin components. This phenomenon is not widely discussed in the fields of epigenetic therapy (15) or chromosome instability in cancer (16), even though such a paradigm might uncover some early drivers of genetic alterations in tumors (17–19). Indeed, it is plausible that some germline-specific genes could induce chromosomal instability (20–22), such as chromothripsis (23–29), but experimental evidence for such a hypothesis was lacking.

The subunits of meiotic cohesin complexes (mei-CC) (30, 31) are of particular interest when activated as CT factors, because their roles in sister chromatid cohesion (SCC) and chromosome pairing in germline are dramatically distinct from the functions of somatic cohesin (32). Nevertheless, the transcriptional activation in tumors is rather common for some mei-CC subunits, which is difficult to reconcile with their toxicity observed in lower eukaryotes (33–36). In the mammalian germline, at least two distinct types of meiosis-specific cohesin complexes, i.e., REC8-based and RAD21L-based, have been reported (37–43). REC8 is present in all eukaryotes and appears to operate in a canonical SCC role: to hold sister chromatids together, especially at centromeres, and to counteract nonhomologous pairing in mouse germline (43, 44). In contrast, RAD21L has evolved only in Metazoa. Genetic studies on mice pointed to a putative role of RAD21L as a facilitator of the initial contacts between homologs (34, 45) and the formation of chromosome axis (44, 46). Cytological data indicate that REC8 loading precedes DNA replication in meiosis I and persists through the metaphase II, while RAD21L is loaded after DNA is replicated and is largely removed before the anaphase I (38). Genetic data show that these two complexes are only partially redundant (40) but are functionally cooperative (44), driving pairing and segregation of meiotic chromosomes (32, 40–42, 46–56).

Author contributions: A.A. and A.V.S. designed research; A.B., J. Liu, Q.W., A.A., and J. Liang performed research; A.A., M.D., V.L., and M.E. contributed new reagents/analytic tools; C.W., A.A., E.M.P., and A.V.S. analyzed data; and A.V.S. wrote the paper.

The authors declare no competing interest.

This article is a PNAS Direct Submission.

[1]To whom correspondence may be addressed. Email: alex@gibh.ac.cn.

This article contains supporting information online at http://www.pnas.org/lookup/suppl/doi:10.1073/pnas.2204071119/-/DCSupplemental.

Published September 30, 2022.

In contrast to the normal germline, the functions of human mei-CC proteins in tumors were not studied in detail (57), despite their prognostic potential (58). Here, based on the interrogation of cancer genomes data, we established a model to study meiotic cohesins outside the constraints of their germ cell environment, i.e., in cancer cell lines, primarily DLD-1, and supplemented that with epigenomic analysis on a normal nonhuman primate testis. Our results indicate that mei-CCs, when reconstituted in the model system, affected gene expression in a distinct fashion, as well as manifested drastically different phenotypes with respect to cell proliferation and chromosome segregation. In particular, the ectopic RAD21L mei-CC expression resulted in a prolonged cell-cycle arrest with a potential to generate severe chromosomal abnormalities, including DNA damage and occasional formation of multistrand chromosomes. In this ectopic system, as well as in primate testis, the REC8 and RAD21L mei-CCs predominately localize to the sites that are occupied by BORIS/CTCFL in the normal germline. Our findings offer a plausible explanation for the low-frequency expression of RAD21L in tumors and demonstrate that experimentally activated CT genes can rapidly impair genome integrity, serving as a potent source of chromosomal instability.

Results

Mei-Cohesin Subunits Display Expression Bias as CT Genes. To make inroads into assessing potential roles of CT genes outside of germline, we first focused on the expression of all core cohesin components (Fig. 1*A*) and the associated cofactors in tumors. TCGA (The Cancer Genome Atlas) RNA-sequencing (RNA-seq) dataset analysis shows that the individual mei-CC subunits form two separate patterns: SMC1B and STAG3 cluster with a number of somatic cohesin components, while RAD21L and REC8 show no correlation with other interrogated genes

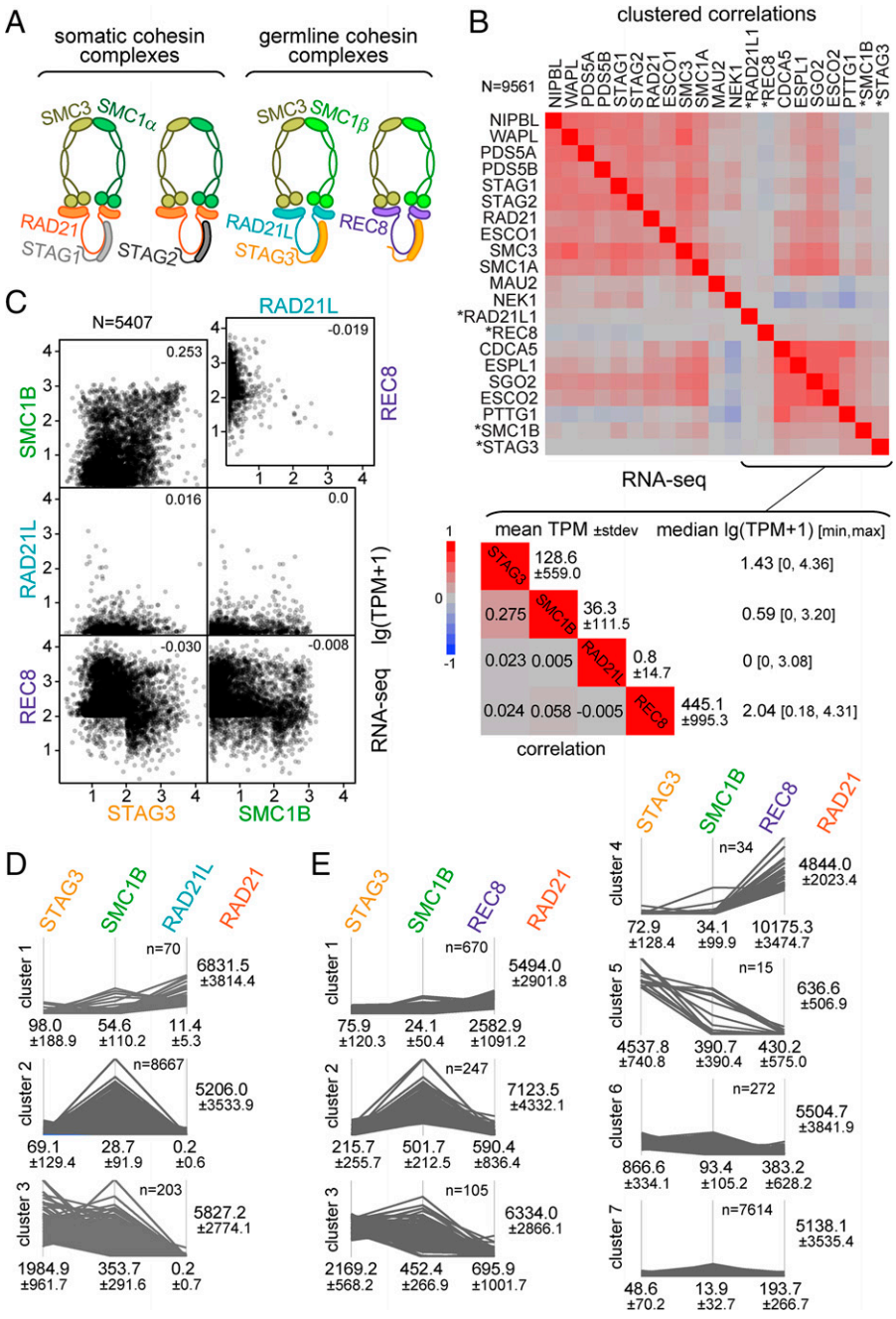

Fig. 1. The overexpression and coexpression of mei-cohesin subunits in tumors. (*A*) A schematic of somatic cohesin complexes compared to mei-CC. (*B*) Multivariate correlation of human cohesin subunits' expression and associated factors in 9,561 samples from TCGA RNA-seq (https://www.cancer.gov/about-nci/organization/ccg/research/structural-genomics/tcga). Heat-map fragment shows mei-CC subunits only, with corresponding correlations in boxes and TPM statistical parameters on the left. (*C*) Scatterplot of relative mei-CC subunits' expression in TCGA. Only nongermline tumors with at least one gene expressed at TPM ≥ 100 are included. (*D* and *E*) Parallel coordinates plots from cluster analysis of nongermline tumors for RAD21L (*D*) and REC8 (*E*) coexpression with SMC1B and STAG3. Only clusters bigger than 10 are shown. The corresponding mean TPM expression values are indicated below. RAD21 is shown for each cluster as a somatic paralogue reference.

(Fig. 1*B*). The mei-CC genes have a wide range of expression levels in different tumors, except RAD21L, for which both the incidence of activation and expression levels are the lowest (Fig. 1 *B* and *C* and *SI Appendix*, Fig. S1*A*). In tumors of nongermline origin, cluster analysis of coexpression with SMC1B and STAG3 revealed that RAD21L expression was either lower than both SMC1B and STAG3 (Fig. 1*D*, cluster 1) or, more commonly, was practically undetectable when SMC1B and/or STAG3 were highly expressed (Fig. 1*D*, clusters 2 and 3). In the case of REC8 such a bias was not evident (Fig. 1*E*).

Thus, we detected some notable deviations from a presumable sporadic mode of activation of mei-CC subunits in tumors. While the expression of neither REC8 nor RAD21L correlated with other mei-CC genes, RAD21L had orders of magnitude lower incidence of activation, as well as lower levels of expression, compared to all other subunits, prevailing through all tumor types (*SI Appendix*, Fig. S1*B*). This parallels the low level of RAD21L messenger RNA detection in normal somatic cells, where other mei-CC subunits are occasionally expressed in a fraction of tissues (*SI Appendix*, Fig. S1*C*) but, as a whole, at substantially lower levels than could be achieved in tumors. This drastically differs from normal germline (*SI Appendix*, Fig. S1 *C* and *D*), indicating that the low expression in tumors is unlikely due to the inherent weakness of RAD21L promoter(s). Furthermore, proteomic data for normal tissues (intensity-based absolute quantification, iBAQ; https://www.proteomicsdb.org/) indicate that RAD21L protein is never detected in soma, while SMC1B peptides, for example, could be detected in 30 normal somatic cell types (59).

Thus, there could be a possibility of a selection in tumors against REC8 and RAD21L coexpression with SMC1B and STAG3, as well as against high expression of RAD21L regardless of other factors. This indicates that RAD21L alone as well as full mei-CC might have a negative effect on cell proliferation, which could be experimentally testable.

Ectopic Expression of RAD21L Mei-CC in Mitotically Dividing Cells Inhibits Cell Proliferation. Based on our survey of TCGA data we set out to investigate the underlying reasons of observed expression biases by expressing human mei-CC subunits in immortalized cells. We generated constructs to stably express ectopic mei-CC subunits and developed specific chromatin immunoprecipitation (ChIP)-grade antibodies to all core mei-CC components (*SI Appendix*, *Supplementary Information Text* and Fig. S2).

The inducible expression of RAD21L and REC8 in a DLD-1 cells model showed that RAD21L, but not REC8, triggered a delay of cell proliferation (Fig. 2*A*). While this phenotype was unlikely due to RAD21L stably replacing somatic RAD21, some dynamic competition between the two for chromatin binding cannot be ruled out (Fig. 2*B*). In contrast, a rather stable binding of RAD21L and REC8 to chromatin was achieved when two other mei-CC subunits, SMC1B and STAG3, were coexpressed (Fig. 2*C*). Furthermore, the coexpression of STAG3 and SMC1B with RAD21L resulted in a stalled proliferation evident as early as 48 h after induction (Fig. 2*D*). These cells, as well as similarly engineered cells without any epitope tags, had most nuclei showing variable degrees of unscheduled chromosome condensation, with RAD21L forming filamentous structures along nuclear DNA (Fig. 2*E*). This effect was not specific for DLD-1 cells, as similarly constructed K562 cell lines also displayed atypical chromosome condensation (Fig. 2*F*) in the majority (83%) of cells (Fig. 2*F*). RAD21L mei-CC cells also displayed a reduced fraction of prometaphases and metaphases (less than 1%). Interestingly, in rare cases (about 0.5%) when relatively normal metaphases with amphitelic attachment of microtubules were seen in RAD21L mei-CC cells, sister centromeres were poorly resolved (Fig. 2*G*), indicating a failure to achieve proper balance of tension at kinetochores. At the same time, the expression of REC8 mei-CC did not show any profound effect on chromatin morphology or cell proliferation (Fig. 2*E*). However, some discernible chromosomal phenotype was observed in metaphase, with up to half of all metaphases having a visibly disorganized kinetochore plate and reduced Aurora B signal at the kinetochores (Fig. 2*H*).

Chromosome Remodeling Induced by RAD21L Mei-CC Is Dependent on Cohesin Ring Complex Formation and Results in a Specific Chromatin and Transcriptome State. The mechanism of severe alteration of chromosomal cycle associated with RAD21L mei-CC in our cell system could be attributed to a direct effect of mei-CC complex assembly and its involvement in chromatin restructuring. Alternatively, it could be a consequence of meiotic genes induction and/or a depletion of endogenous cohesin due to competition. To confirm that the mei-CC complexes were indeed assembled in vivo, we reengineered the triple transgenic cell lines so that FLAG tag was present only on REC8 or RAD21L. IP with anti-FLAG antibodies demonstrated that the expected complexes were indeed assembled (*SI Appendix*, Fig. S3*A*). To test whether the cohesin ring structure of RAD21L mei-CC itself is required, we again redesigned cell lines, replacing RAD21L with two proteolytically cleavable, i.e., P2A peptide-containing (60, 61), versions of RAD21L: RAD21L-P2A^{178} and RAD21L-P2A^{231}. The RAD21L-P2A mei-CC complexes did assemble in vivo, arguing that in our system the P2A auto-cleavage is mediated mainly through host proteolytic cleavage, and were bound to chromatin (Fig. 3*A*). However, RAD21L-P2A mei-CC did not result in chromosomal or cell-cycle defects induced by the corresponding intact mei-CC (Fig. 3*B*), strongly indicating that the ring structure of RAD21L mei-CC is crucial for the observed phenotypes.

To characterize chromatin states induced by RAD21L mei-CC by quantitative means we conducted Assay for Transposase-Accessible Chromatin with high-through put–sequencing (ATAC-seq) analysis (62). Among accessible chromatin locations present in control, RAD21L mei-CC showed a substantially higher number of sites with reduced accessibility (Fig. 3*C*). However, some sites did become more open, and new accessible locations appeared (Fig. 3*C*). This signifies a programmed remodeling of epigenomic state in these cells. Overall, 30,200 peaks had at least 1.5 times change in accessibility, of which 8,652 were regulatory elements, i.e., promoters or enhancers.

It was highly probable that chromatin remodeling induced by RAD21L mei-CC would result in specific changes of gene expression. Therefore, we carried out transcriptome analysis by RNA-seq of four types of cell lines: DLD-1 control, DLD-1$^{SMC1B\text{-}STAG3}$, DLD-1$^{SMC1B\text{-}STAG3\text{-}REC8}$, and DLD-1$^{SMC1B\text{-}STAG3\text{-}RAD21L}$ (Fig. 3 *D* and *E* and *SI Appendix*, Fig. S3*B*). The expression of mei-CC subunits genes in the DLD-1 was on the level of background: SMC1B 3.7 ± 4.0, STAG3 111.7 ± 123.4, REC8 40.3 ± 36.5, and RAD21L 0.0 Transcripts per Million (TPM), with endogenous RAD21 reaching 2,270.7 ± 2,455.1 TPM. The ectopic expression of the transgenes (SMC1B 4,495.4 ± 3,145.1, REC8 17,755.3 ± 6,713.8, and RAD21L 3,782.7 ± 467.1 TPM) somewhat exceeded the latter but largely corresponded to the expression of RAD21 in tumors (Fig. 1 *D* and *E*), while being higher than in developed tumors in TCGA dataset (Fig. 1*B*). DLD-1$^{SMC1B\text{-}STAG3}$ cells had no differentially expressed genes (DEGs), except a mild increase in IL18. DLD-1$^{SMC1B\text{-}STAG3\text{-}REC8}$ cells had 45 DEGs, with only EEFA2 notably overexpressed (Fig. 3*E*). RAD21L mei-CC cells had

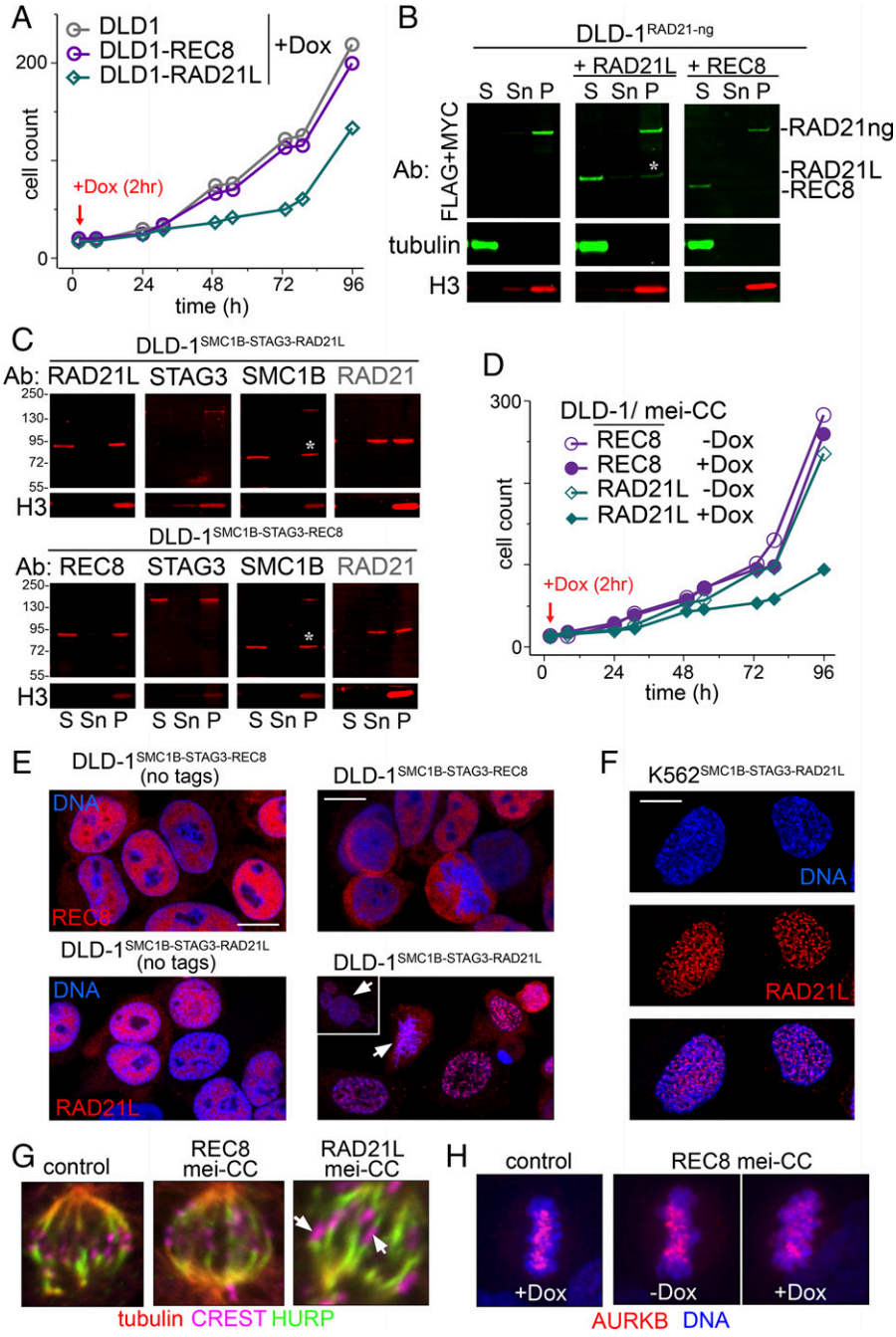

Fig. 2. RAD21L and REC8 mei-CC complexes have differential effects on cell proliferation and chromatin morphology. (*A*) Growth curves for DLD-1, DLD-1^{RAD21L}, and DLD-1^{REC8} single clones. (*B*) Analysis of the competition of ectopic RAD21L and REC8 with the endogenous RAD21-neonGreen fusion. Soluble (S), nuclear soluble (Sn), and chromatin pellet (P) fractions of DLD-1$^{RAD21-ng}$ stably expressing inducible RAD21L or REC8 were probed with anti-FLAG (recognizes RAD21-ng and RAD21L) and anti-myc (recognizes REC8) antibodies. Asterisk indicates a partial retention of RAD21L in chromatin. (*C*) Chromatin fractionation of DLD-1 coexpressing SMC1B, STAG3, and RAD21L (*A*) or SMC1B, STAG3, and REC8 (*B*) induced for 96 h. Fractions are as in *B*. Asterisks mark a proteolytic breakdown band. (*D*) Growth curves for DLD-1, DLD-1$^{SMC1B-STAG3-RAD21L}$, and DLD-1$^{SMC1B-STAG3-REC8}$ single clones, with and without doxycycline (Dox). (*E*) IF for REC8 and RAD21L in asynchronous triple transgenic DLD-1 with induced mei-CC. REC8, RAD21L, SMC1B, and STAG3 expressed either as untagged proteins (*Left*) or epitope-tagged (*Right*). Arrows point to a cluster of micronuclei (*Inset*) and a disorganized mitosis in RAD21L mei-CC cells. (Scale bars, 10 μm throughout.) (*F*) IF of K562$^{SMC1B-STAG3-RAD21L}$ cells induced for 72 h. Images are confocal projections. (*G*) Comparison of anaphase kinetochore and spindle structures in DLD-1 (control), DLD-1$^{SMC1B-STAG3-REC8}$, and DLD-1$^{SMC1B-STAG3-RAD21L}$. Arrows point to stretched unresolved kinetochores. (*H*) Comparison of metaphases in DLD-1 (control) and DLD-1$^{SMC1B-STAG3-REC8}$.

the largest signature of 210 DEGs. Their comparison to the significantly affected preleptotene genes in mouse (63) revealed an overlap of 63 genes. Similarly, a comparison to a human germline development dataset (64) revealed a concordant increase for 11 genes: AREG, BMI1, HIST1H1C, HLA-B, MYADM, NPC2, OPTN, PLK2, PSMD1, SCML1, and SQSTM1. Overall, among transcription start sites (TSS) of genes differentially regulated in RAD21L mei-CC cells there was a good correspondence with ATAC-seq data (Fig. 3*F*).

Thus, it is likely that RAD21L mei-CC directly restructures chromosomes in a specific manner inducing the downstream cell-cycle phenotype. Still, we could not exclude a possibility that it also down-regulated some somatic chromosome components posttranscriptionally. However, proteome analysis demonstrated no dramatic protein level change among 6,889 detected proteins (Dataset S1) that could be associated with the phenotype of RAD21L mei-CC cells. For example, only two proteins, ANKRD22 and SULT1A3, both unrelated to chromosome function, were down-regulated more than twofold among relevant KEGG (Kyoto Encyclopedia of Genes and Genomes) pathways. Particularly, apart from moderately decreased SMC1A, which is functionally interchangeable with SMC1B (51), the abundance of somatic cohesin, condensin, and associated factors was not significantly affected either (Fig. 3*G*).

The Specificity of DNA Binding by Ectopic Mei-Cohesin Reflects a Germline Pattern. In order to investigate the in-depth properties of chromatin that was exposed to mei-CC in nongermline cells we assessed mei-CC binding to chromatin, beginning with individual subunits. First, we focused on K562 cells, which express another Cancer Testis Antigen (CTA), BORIS, a meiotic partner of CTCF, known to immobilize somatic cohesion at a

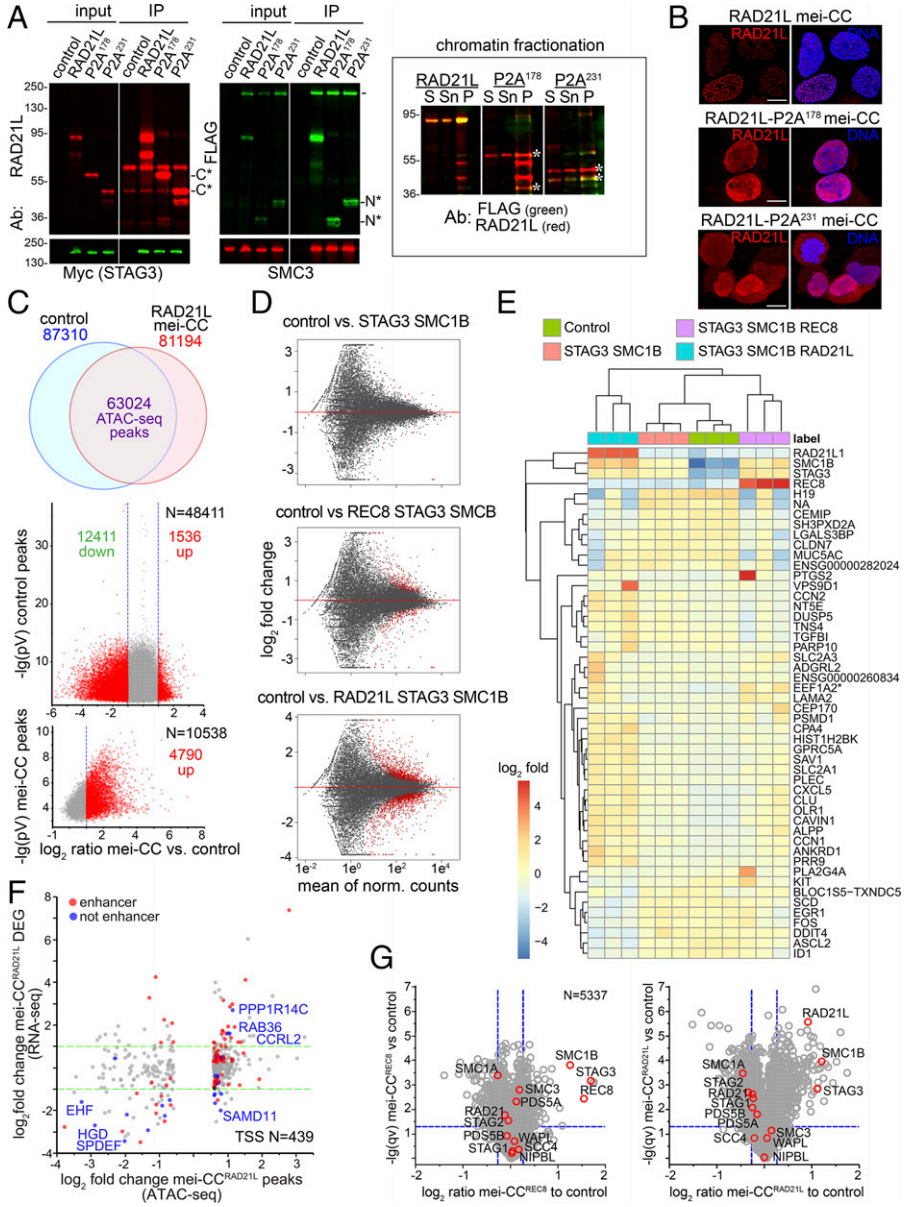

Fig. 3. Ectopic RAD21L and REC8 mei-CC complexes induce distinct chromosome phenotypes and transcriptional response. (*A*) Analysis of RAD21L-P2A cleavage in vivo. Two variants of DLD-1$^{SMC1B\text{-}STAG3\text{-}RAD21L\text{-}P2A}$, DLD-1$^{SMC1B\text{-}STAG3\text{-}RAD21L}$, and DLD-1 (control) cells were induced for 72 h. The amino and carboxyl-terminal proteolytic fragments are marked with N* and C* in the left panel (RAD21L Ab IP) and with asterisks in the right panel (chromatin fractionation). Anti-FLAG Ab were included to reliably identify short N-terminal fragments. (*B*) IF of induced(72 h) DLD-1$^{SMC1B\text{-}STAG3\text{-}RAD21L}$ and DLD-1$^{SMC1B\text{-}STAG3\text{-}RAD21L\text{-}P2A}$ stained for RAD21L. (Scale bars, 10 μm throughout.) (*C*) ATAC-seq of DLD-1$^{SMC1B\text{-}STAG3\text{-}RAD21L}$ compared to DLD-1 control. The chart represents all peaks in the two cell lines. Density plots below are for nonrepeat centered peaks <1 kb, either present in both datasets (*Top*) or in mei-CC cells only (*Bottom*). (*D*) MA plots from RNA-seq of DLD-1$^{SMC1B\text{-}STAG3}$, DLD-1$^{SMC1B\text{-}STAG3\text{-}RAD21L}$, DLD-1$^{SMC1B\text{-}STAG3\text{-}REC8}$, and DLD-1. Induction 72 h. For DLD-1$^{SMC1B\text{-}STAG3\text{-}RAD21L}$ DEGs included regulatory proteins: kinases and their cofactors *PLK2*, *MAP3K14*, *ERBB3*, *EPHA2*, *LATS2*, *STK17A*, and *PEA15*; phosphatases *PPP1R15A*, *DUSP6*, and *DUSP5*; chromatin components *H2BFS*, *HIST1H2BK*, *HIST1H1C*, *HMGA2*, *MRNIP*, and *BMI1*; cytoskeleton components *KIFC3*, *TUBB6*, *TUBB2A*, and *PLEC*; and apoptotic hippo pathway components *LATS2*, *STK17A*, and *SAV1*. (*E*) A heat map of differential expression for 50 most affected genes in all RNA-seq experiments combined. (*F*) Correspondence of ATAC-seq and RNA-seq for 439 TSS of affected genes; 326 sites are also qualified as enhancers (GeneHancer), and 98 significant DEGs are highlighted, with some example genes. (*G*) Proteome analysis of DLD-1$^{SMC1B\text{-}STAG3\text{-}REC8}$, DLD-1$^{SMC1B\text{-}STAG3\text{-}RAD21L}$, and DLD-1 cells by iTRAQ mass spectrometry. Volcano plots only include proteins with more than one unique peptide. Cohesin pathway proteins are highlighted in red. Significance thresholds (vertical blue lines) correspond to 1.2 times fold change and the horizontal blue line is 0.05 q-value. Induction for 72 h.

given site (65–67). While SMC1B showed a strong presence in fractionated chromatin, REC8, RAD21L, or STAG3 had only marginal chromatin association (*SI Appendix*, Fig. S4*A*). The follow-up by ChIP-on-ChEP (Chromatin Enriched for Proteomics)-seq analysis confirmed that RAD21L and REC8 gave only negligible number of nonrepeat peaks, all with low scores. SMC1B, however, gave 28,740 nonrepeat summit peaks, and 4,916 peaks were also uncovered for STAG3. While SMC1B was largely coincident with CTCF binding (*SI Appendix*, Fig. S4*B*), possibly as a result of exchange with somatic SMC1A, STAG3 was predominately associated with robust BORIS-occupied sites and absent from CTCF-only sites (*SI Appendix*, Fig. S4 *B* and *C*). At the same time, the occupancy of SMC1B showed a meaningful correlation with CTCF occupancy, while STAG3 tag density displayed no correlation with BORIS occupancy levels (Fig. 4*A*). In order to test whether STAG3 merely recognizes sites common with BORIS or BORIS itself, we introduced an inducible *STAG3* into two additional cell lines: DLD-1 and RPE-1, where BORIS expression is silenced. Of the combined STAG3 peaks in these two cell lines, the absolute majority was overlapping with peaks identified in K562, except only about ∼500 locations, confirming that STAG3, albeit weakly, can bind chromatin independently of BORIS, with the strongest correlation to the TSS (Fig. 4*B*).

In contrast, for triple transgenic mei-CC cell lines ChIP-on-ChEP-seq revealed a prominent pattern of cobinding of mei-CC subunits genome-wide (Fig. 4*C*), with REC8 and RAD21L both strongly correlating with SMC1B and STAG3 binding (Fig. 4*C*). This indicates that the presence of the full four-subunit core mei-CC enables it to bind chromatin specifically (e.g., *SI Appendix*, Fig. S4*D*). When analyzed for each subunit individually, the genome-wide distribution of mei-CC binding sites showed a notable relative depletion of intergenic sequences (*SI Appendix*, Fig. S4*E*). Both REC8 mei-CC and RAD21L mei-CC showed almost complete cobinding with CTCF (*SI Appendix*, Fig. S4*F*), as well as a substantial enrichment at promoters and enhancers.

The revealed pattern of mei-CC binding, despite small differences, indicated that both ectopic REC8 and RAD21L mei-CC followed the general pathway of somatic cohesin binding, i.e., association with CTCF. Therefore, we asked whether such mei-CC association with DNA in DLD-1 cells is reminiscent of germline patterns. In the absence of ChIP-seq–grade human

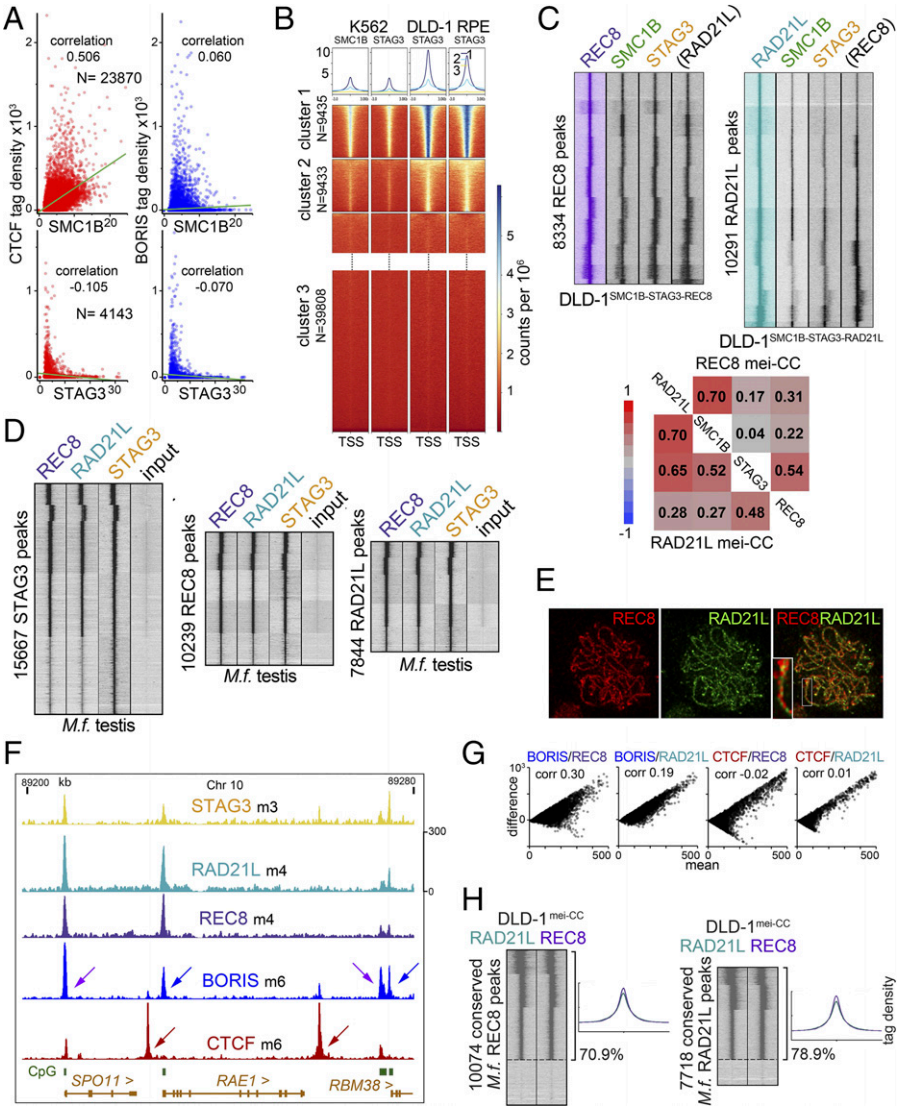

Fig. 4. Epigenomics of ectopic and native mei-CC expression. (*A*) Correlation of SMC1B but not STAG3 binding with CTCF in K562. Normalized tag densities for 200-bp windows centered at peak summits for ectopic STAG3 and SMC1B after 96-h induction were correlated with the endogenous BORIS and CTCF. SMC1B with CTCF correlation is meaningful ($P < 0.0001$) and STAG3 correlates with neither BORIS or CTCF. (*B*) STAG3 binds at TSS independently of BORIS. STAG3 ChIP-on-ChEP-seq for BORIS-negative DLD-1 and RPE-1 cells showed 40,105, and 52,528 nonrepeat peaks, respectively, with 18,061 common peaks. Combined tag densities and corresponding heat maps are shown for three distinct clusters. (*C*) Correlations of mei-CC DNA binding in triple-transgenic DLD-1. Shown are normalized ChIP-seq tag density heat maps for REC8 and RAD21L mei-CC DLD-1 cell lines induced for 96 h. Tag densities were plotted for 6-kb intervals centered at superset peak summits. Reciprocal densities for RAD21L and REC8 are for comparison. Correlation heat map below corresponds to the normalized (41×10^6 reads per dataset) tag densities for 400 bp centered at the peaks above. (*D*) Colocalization of mei-CC subunits in macaque testis. Heat-map parameters as in *C*. The same number of aligned clean reads plotted for each experiment. (*E*) REC8 and RAD21L partially overlap on chromosomes in meiotic prophase I. Testis cells preparation from *M. fascicularis* was subjected to Cytospin before IF. (*F*) Examples of ChIP-on-ChEP-seq peaks in monkey testis. The 80-kb region in *SPO11* vicinity represents different types of CTCF and BORIS enriched peaks and corresponding binding for mei-CC subunits. Signal scale is uniform for all tracks. (*G*) The strength of mei-CC binding in testis correlates with BORIS. Normalized tag densities are plotted for BORIS and CTCF versus REC8 and RAD21L peaks. Correlations (corr) are based on pairwise comparison. (*H*) Binding of RAD21L and REC8 in triple-transgenic DLD-1 resembles their epigenomic distribution in testis. Supersets of *M. fascicularis* peaks for RAD21L and REC8 were converted to human (hg38) coordinates, and the corresponding summit-centered 6-kb windows were analyzed for RAD21L and REC8 normalized tag density in DLD-1$^{SMC1B\text{-}STAG3\text{-}RAD21L}$ and DLD-1$^{SMC1B\text{-}STAG3\text{-}REC8}$.

testis material we investigated the pattern of mei-CC binding in the spermatogenesis of *Macaca fascicularis*. Recent single-cell RNA-seq studies documented uniqueness of gene expression programs in primate testis (64, 68, 69). *M. fascicularis* has reproductive biology similar to humans, a substantial collinearity to human genome, and high homology of its mei-CCs to human ones; 10,239 high-confidence testis peaks were mapped by ChIP- on-ChEP-seq for REC8, 7,844 for RAD21L, and 15,667 for STAG3 (Fig. 4*D* and *SI Appendix*, Fig. S5*A*). The STAG3 ChIP had a weaker enrichment with higher noise, while SMC1B consistently gave low signal, with only 6,042 peaks identified in the best replicate. Therefore, the SMC1B peaks were not analyzed further. A consistent cooccupancy between the three mei-CC subunits was evident (Fig. 4*D* and *SI Appendix*, Fig. S5*A*) and the strength of RAD21L and REC8 binding was well correlated (*SI Appendix*, Fig. S5*B*). The latter was most likely due to compounding of signal for the two mei-CC complexes considering single cell RNA sequencing (scRNA-seq) data (68, 69), immunofluorescence (IF) (Fig. 4*E*), and cross-linked chromatin co-IP experiments (*SI Appendix*, Fig. S5*C*).

We also employed ChIP-on-ChEP-seq to investigate mei-CC relationship with CTCF and BORIS, as scRNA-seq data from human and macaque testis indicated only partial coexpression of BORIS with mei-CC in the course of spermatogenesis, with CTCF expressed throughout (64, 68, 69); 21,165 high-confidence peaks for BORIS and 31,547 peaks for CTCF were identified, with 15,788 peaks that could be considered CTCF-only (*SI Appendix*, Fig. S6 *A* and *B*). Of BORIS peaks common to two samples 36.4% overlapped with TSS. In contrast, only 13.3% of CTCF peaks overlapped with TSS. Intriguingly, the mei-CC subunits' peaks substantially coincided with BORIS binding (Fig. 4*F* and *SI Appendix*, Fig. S6*C*), and the strength of mei-CC and BORIS peaks was correlated, unlike with CTCF (Fig. 4*G*). Peak annotations indicated that mei-CC subunits were enriched in transcription control regions (*SI Appendix*, Fig. S7*A*), with corresponding Gene Ontology (GO) analysis showing a wide range of corresponding biological processes (*SI Appendix*, Fig. S7*B*).

Thus, BORIS binding could be a prerequisite for mei-CC positioning, as its expression precedes mei-CC emergence in the spermatogenesis (64, 68, 69). This is supported by our IF results (*SI Appendix*, Fig. S6*D*) and the proteomics (mouse protein atlas, https://www.ebi.ac.uk), which places the bulk of BORIS into spermatogonia. Our analysis of fluorescence-activated cell sorting (FACS)-purified cell fractions also indicated that the difficult to isolate (70) premeiotic germline cells evidently generated the bulk of IF BORIS signal (*SI Appendix*, Fig. S6 *E*–*G*). Nevertheless, round spermatids and spermatocytes still showed a notable correspondence of mei-CC binding (analyzed for REC8) to BORIS sites (*SI Appendix*, Fig. S6*H*).

Available data indicate that BORIS functions predominately as a transcription factor (64, 71). Therefore, while it appears to mark sites of mei-CC binding, the exact molecular role of BORIS there is not clear, especially as mei-CCs are able to associate with chromatin in BORIS knockout (KO) mice (72). To get more insight into this, we analyzed the landscape of H3K27ac binding in *M. fascicularis* testis. ChIP-on-ChEP-seq analysis showed 20,849 high-confidence gene-overlapping peaks, with the stronger ones substantially overlapping with both REC8 and RAD21L (*SI Appendix*, Fig. S8*A*). A much smaller number of H3K27ac sites that did not overlap with any genes, i.e., likely at enhancers, showed a similar pattern. However, a significant difference with BORIS was evident, with mei-CC peaks overlapping H3K27ac signal, but with distinct summits (*SI Appendix*, Fig. S8*B*). Therefore, it likely that BORIS coincides with mei-CC due to its engagement in chromatin remodeling related to transcription. This, in turn, could be a reason for a prominent correspondence of mei-CC meiotic binding to the pattern seen in cell lines. Indeed, over 70% of REC8 and RAD21L peaks in these cell lines overlapped with their corresponding conserved sites in macaque testis (Fig. 4*H*).

The Ectopic Expression of Full Mei-Cohesin Complexes Reveals a Plausible Mechanism of RAD21L Toxicity and Underrepresentation in Tumors. As we established that binding of RAD21L mei-CC in tested cell lines is reminiscent of germline pattern, we investigated the phenotype induced by the ectopic RAD21L mei-CC in more detail. The RAD21L filament-like structures assembled along chromosomes in RAD21L mei-CC cells eventually spanned the entire length of individual chromosomes, from centromeres to telomeres, notably excluding ribosomal DNA (rDNA) chromatin, well before nuclear envelope breakdown (Fig. 5*A*). The corresponding chromosome condensation was not induced by mitotic commitment, as it did not correlate with phoshpho-S10-H3 signal (Fig. 5*B*). As the RAD21L-containing filaments were somewhat reminiscent of somatic cohesin deposition upon the inactivation of prophase pathway for cohesin removal (73, 74), we knocked down WAPL machinery in RAD21L mei-CC cells (Fig. 5*C*). The atypical condensation phenotype in RAD21L mei-CC cells appeared to be epistatic to prophase pathway (Fig. 5*D*).

The investigation of mei-CC cells presynchronized by double thymidine block revealed additional prominent defects in RAD21L mei-CC–expressing cells, such as stretched centromeres in interphase (Fig. 5*E*) and ubiquitous gamma-H2AX foci in anaphase cells, indicative of chromosome breaks (Fig. 5*F*). Also, the condensin complex, condensin I in particular, was not properly covering the length of chromosome arms (75) but instead was showing an interleaving pattern of binding with RAD21L (Fig. 5*G*). Synchronized cells revealed that the control, REC8, and RAD21L mei-CC cell lines did not have a major delay of S phase for two doubling times, according to BrdU FACS data (Fig. 5*H*). The synchronization (Fig. 5*I*) also showed that RAD21L mei-CC did not induce chromatin condensation before the beginning of S phase (0 h) but that the filaments appeared to fully assemble on condensed chromatin by the end of S phase (6 h) (*SI Appendix*, Fig. S9*A*), indicating that a passage through DNA synthesis was required for RAD21L mei-CC loading. Gamma-H2AX staining in the synchronous cell population indeed revealed that the initial loading of RAD21L coincided with replicating DNA (*SI Appendix*, Fig. S9*B*). Furthermore, after the completion of S phase the centromeres were unusually stretched or improperly condensed before nuclear envelope broke down (*SI Appendix*, Fig. S9*C*). The kinetic of following mitosis was, however, drastically different for REC8 and RAD21L mei-CC cell lines: While REC8 cells had a delayed anaphase, consistent with a kinetochore defect (Fig. 2), RAD21L cells not only had a delay entering mitosis but also largely failed to complete the passage through mitosis altogether, with only about one fifth of population initiating chromosome segregation at the 12-h time point (Fig. 5*I*). In RAD21L mei-CC cells, the dynamic of cyclin B1 (Fig. 5*J*) was also consistent with a mitotic exit block. While some RAD21L cells did reach metaphase, with the bulk of RAD21L leaving the condensed chromosomes (Fig. 5*F* and *SI Appendix*, Fig. S9*D*), all the detected anaphases had either chromosomal bridges or multiple gamma-H2AX foci, or both (*SI Appendix*, Fig. S9 *B* and *E*). The rest of the cell population appeared to be blocked in G2-M-like state and maintained high viability, above 80%, in the virtual absence of proliferation.

In order to determine the execution point of RAD21L mei-CC–induced arrest, cells were synchronized by an alternative regimen: first prearrested in S phase and then released into a G2 block with simultaneous induction of RAD21L mei-CC (*SI Appendix*, Fig. S9*F*). As the ectopic proteins levels peaked 4h after induction, this approach enabled cells to reach the end of S phase before encountering the full expression of RAD21L mei-CC. These cells did not show interphase condensation induced by RAD21L cohesin (*SI Appendix*, Fig. S9*G*) and had no apparent delay in entering metaphase (*SI Appendix*, Fig. S9*H*). However, at later points these cells showed signs of a defective mitotic completion—prolonged chromosome condensation, collapsed or asymmetrical spindles, and centromeres trapped at the division furrow (*SI Appendix*, Fig. S9*I*)—while control cells have exited mitosis by that point (*SI Appendix*, Fig. S9*J*) and had the expected centromere counts per cells (*SI Appendix*, Fig. S9*K*). These data suggest that RAD21L cohesin interferes with centromere function within mitosis, even when abnormal S-phase condensation is avoided.

An additional observation suggested that the RAD21L mei-CC filament assembly has a meiotic-like physiological role. Namely, a small fraction of cells (about 1/250) expressing ectopic RAD21L mei-CC had chromosomes that were substantially thicker than normal. While such cells had interphase-like nuclei and microtubule arrangement, IF revealed either a paired appearance for each RAD21L filament (Fig. 5*K*), similar to condensin cores in normal metaphases (76), or multiple DNA strands aligned in a parallel fashion (Fig. 5*L*), as well as more than two aligned centromeres (Fig. 5*M*). Such cells contained on average 145 CREST spots, which is more than double the number expected for this quasi-diploid cell line, i.e., likely became tetraploid. This indicates that RAD21L cohesin has an ability to promote formation of multi-strand chromosomes and to keep multiple chromatids aligned together, suggesting that this complex maintains, and likely initiates, chromosome pairing in the absence of meiotic factors.

It was also of substantial interest to understand what happens to RAD21L cohesin cells that do not complete mitosis, i.e., a majority in the arrested population. To address that we conducted long-term time-course experiments, where induced RAD21L mei-CC cells were passaged for nearly 2 wk and then released from the induction (*SI Appendix*, Fig. S10*A*). Under that protocol, most arrested cells showed RAD21L-stained condensed chromosomes in the nucleus; however, 28% of cells had micronuclei (day 9; *SI Appendix*, Fig. S10*B*). The latter is a probable indication of abortive mitosis still proceeding in a fraction of this population, serving as an "engine" producing genetically altered cells and explaining the lower than 100% viability (*SI Appendix*, Fig. S10*A*). Upon removal of mei-CC

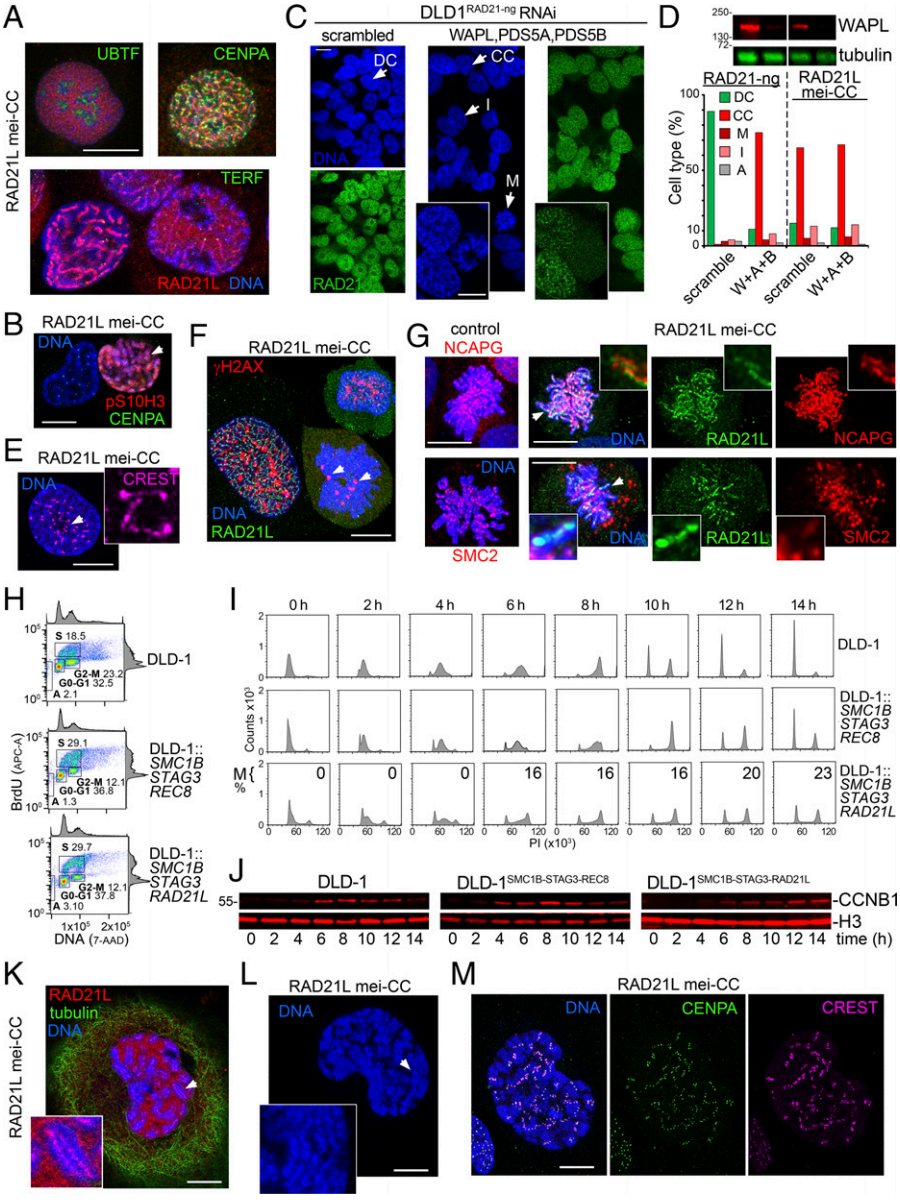

Fig. 5. Cell cycle and chromosomal phenotypes due to ectopic mei-CC expression. (*A*) IF of markers for nucleolar chromatin (UBTF), centromere (CENPA), and telomere (TERF) for DLD-1$^{SMC1B\text{-}STAG3\text{-}RAD21L}$. (*B*) IF staining for phospho-S10 H3 histone epitope in DLD-1$^{SMC1B\text{-}STAG3\text{-}RAD21L}$ cells. (*C*) Microscopy of DLD-1$^{RAD21\text{-}ng}$ treated with siRNA against WAPL, PDS5A, and PDS5B. The examples of cell type categories are marked: CC, condensed chromosomes; IC, intermediate condensation; DC, decondensed chromatin; M, mitotic cells. (*D*) Quantification of DLD-1$^{RAD21\text{-}ng}$ cells treated with siRNA against WAPL, PDS5A, and PDS5B, compared to DAPI-stained DLD-1$^{SMC1B\text{-}STAG3\text{-}RAD21L}$ cells. Classes are as in *C*. A, apoptotic-like cell. (*E*) IF of DLD-1$^{SMC1B\text{-}STAG3\text{-}RAD21L}$ cell immediately after the release from the second thymidine block stained with anti-RAD21L and CREST Abs. Arrows point to stretched centromeres (*Inset*). Figures *E*–*G* and *K*–*M* are flattened confocal images, with deconvolution. (*F*) DLD-1$^{SMC1B\text{-}STAG3\text{-}RAD21L}$ cells, stained with anti-γH2AX and RAD21L Abs. Arrows indicate γH2AX signal persisting in mitosis. (*G*) RAD21L mei-CC interferes with condensin binding in mitotic chromosomes. IF of DLD-1$^{SMC1B\text{-}STAG3\text{-}RAD21L}$ cells shows an alternating pattern of RAD21L, SMC2, and NCAPG in compacted mitotic chromosomes. Insets are at 4× magnification. Control is DLD-1. (*H*) FACS plot of BrdU label versus total DNA fluorescence signal for DLD-1 (control) cell line, DLD-1$^{SMC1B\text{-}STAG3\text{-}RAD21L}$ and DLD-1$^{SMC1B\text{-}STAG3\text{-}REC8}$ cells induced by doxycycline (Dox) for 48 h and then labeled by BrdU for 3 h. Percentages correspond to indicated G0–G1, S, G2–M, and A (apoptotic) gates. (*I*) FACS (cell counts versus PI fluorescence signal) for a time course of synchronous populations of DLD-1 (control), DLD-1$^{SMC1B\text{-}STAG3\text{-}RAD21L}$, and DLD-1$^{SMC1B\text{-}STAG3\text{-}REC8}$ cell lines induced by Dox during the first thymidine block. Time 0 is the release from the second thymidine block. M, the percentage of cells in mitosis, as determined by phospho-S10-H3 staining. (*J*) Immunoblotting of the extracts from the three cell lines in *I*, probed with anti-Cyclin B antibody (CCNB1). Histone H3 is a loading control. (*K*) IF of DLD-1$^{SMC1B\text{-}STAG3\text{-}RAD21L}$ cell at the 2-h time point after the release from the second thymidine block, stained for RAD21L and alpha-tubulin. The arrow corresponds to 4× inset. (*L*) DAPI staining of a DLD-1$^{SMC1B\text{-}STAG3\text{-}RAD21L}$ cell after 72-h induction showing multiple aligned strands of condensed chromatin. (*M*) Anti-CENPA and CREST Abs IF of DLD-1$^{SMC1B\text{-}STAG3\text{-}RAD21L}$ cell, as in *L*. The aligned arrangement of condensed chromosomes displays four individualized centromeres juxtaposed in linear fashion in many cases. (Scale bars, 10 μm throughout.)

induction, the population had returned to normal viability levels and resumed proliferation (*SI Appendix*, Fig. S10*A*). This result might be viewed as a model of a process inducing chromosome instability in normal human cells, i.e. hypothetical RAD21L mei-CC activation followed by its subsequent repression and the resumption of proliferation of genetically altered cells.

Discussion

A Low Incidence of CT Expression in Cancers as a Putative Sign of Their Biological Impact. This study was based on a hypothesis on potential roles of CT genes in chromosome instability, which is frequently associated with early tumorigenesis. Namely, we uncovered a surprisingly low incidence of *RAD21L1* activation and its low expression in human tumors, a notable outlier with respect to wide ranges of CT genes' expression in cancers (2, 3). As a result of the investigation into the potential mechanisms behind that phenomenon, both in primate testis and in human cells in vitro, we elucidated genome-wide processes that likely make RAD21L expression undesirable for tumor-cell proliferation.

The bulk of information on mei-CC interactions with chromatin in germline came from studies in mice, which are substantially different from primates in their spermatogenesis (77–80) and the corresponding gene expression program (68, 69, 81). While the RAD21L mei-CC is not required for SCC per se (56), some functional overlap exists between the REC8 and RAD21L mei-CCs (42), and there is a phase of physical cohabitation between the two complexes, e.g., from leptotene to pachytene (38). Our ChIP-on-ChEP-seq data from macaque testis indicates that binding of REC8 and RAD21L is largely overlapping (Fig. 4). This probably manifests their inherent ability to recognize the same sites rather than physical cobinding, as cytologically they appear in an interleaving pattern and no physical interaction between them was detected in our or any other study.

The ultimate positioning of somatic cohesin in the epigenome is believed to be determined by CTCF (65, 67, 82–93) and WAPL (94). The sites of CTCF and cohesin cobinding (66, 95) contribute synergistically to the formation and maintenance of CTCF-anchored loops and TAD boundaries (85, 88). Nevertheless, a notable fraction of mouse testis mei-CC sites does not coincide with CTCF (80), which could be partially due to limitations of a traditional ChIP technique (96–98) underreporting peaks from densely packed chromatin (99, 100). However, it

may also indicate a participation of another factor specific for spermatogenesis, such as BORIS. While BORIS is unable to position somatic cohesin (67), it might function to preset mei-cohesin patterns in leptotene in a physiologically relevant environment and with its maximal expression (101). Furthermore, only a handful of testis genes responded differentially to BORIS KO in mice (72, 102,103), suggesting that BORIS has an additional role. Accordingly, in macaque germline, we observed that BORIS-bound sites were more numerous than in BORIS-expressing cell lines and detected a substantially more evenly split groups of peak types: BORIS-only, CTCF+BORIS, and CTCF-only, versus ∼1:2.5:6 in cancer cells (10). Analysis of H3K27ac enrichment has revealed a substantial overlap between mei-CC sites and active chromatin, reinforcing the possibility that BORIS presets sites for mei-CC binding.

In K562 cells, SMC1B had a significant cobinding with CTCF sites, while STAG3 was preferentially found at open chromatin sites, including TSS, in all three tested cell lines: K562, DLD-1, and RPE-1. As STAG3 does have a predicted CTCF-interacting motif but no known DNA contacts, we could hypothesize that some cohesin-loading factors could be involved (67, 94). REC8 and RAD21L were unable to bind chromatin on their own or directly compete with the bulk of RAD21 of somatic cohesin (Fig. 2*B*), even though in late pachytene RAD21 apparently displaces RAD21L (38, 39), which also has a CTCF-interacting-like signature S^{308}KVIHKQL. Therefore, RAD21L expression without mei-CC partners could still be under negative selection in soma.

RAD21L expression in tumors also stands out compared to other mei-CC genes, as it does not correlate with the expression of any human transcription factors/cofactors up-regulated in testis (*SI Appendix*, Fig. S10*C*). This is unlike SMC1B and STAG3 that have five common regulatory factors among the top 10 correlations in human tumors (*SI Appendix*, Fig. S10*C*).

The fact that RAD21L complex, as well as REC8 mei-CC, showed robust chromatin binding with a pattern resembling their germline binding in macaque (Fig. 4*H*) indicates the existence of inherent mei-CC activity enabling the recognition of specific genomic or epigenomic sites. As such binding is originally designed for the germline, it might present substantial risks to other cell types.

The Ectopic Expression of RAD21L Mei-Cohesin Reveals a Self-Contained Activity Likely Relevant for Meiosis. In meiosis, RAD21L mei-CC engages in forming chromosome axis and homologous pairing uncoupled from synaptonemal complexes (SC) and double strand breaks (DSB) formation (104–107). Indeed, double *Rad21L Spo11* KO, but not *Rec8 Spo11* KO, lacks homolog pairing (45), while the SC could join only non-homologous chromosomes in *Rad21L* KO (48). We showed that RAD21L mei-CC expression in mitotically dividing cells led to chromatin changes resembling "vermicelli" chromosomes proposed to underpin the formation of interphase chromosome territories (65, 108) and to a prolonged retardation of cell division, with a fraction of cells breaking through to undergo catastrophic mitosis. Furthermore, the establishment of putative "illegitimate" links in chromatids generating suprachromosomal structures (Fig. 5) suggests that ectopic RAD21L mei-CC executes a fragment of a normal meiotic pathway, such as from early leptotene to early pachytene (45). Indeed, while mei-CC axes formation in meiosis facilitates homologs' alignment, essentially bypassing a search for DNA homology, the actual availability of true homologs is not necessary for such an activity (45). The latter signifies an autonomous axis-building activity of RAD21L mei-CC, as well as explains why RAD21L filaments formed in our experiments without chromatin pairing.

While RAD21L mei-CC expression did not have a significant effect on DNA replication progression (Fig. 5), the induction of histones and apoptotic genes, the presence of abundant mitotic staining for gamma-H2AX, as well as a frequent emergence of small nuclei, were indicative of DNA damage in cells breaking through the G2-M arrest. Such a damage likely directly results from DSB in anaphase, as gamma-H2AX foci were observed in every anaphase cell. However, damage could also be linked to one of meiotic functions of RAD21L mei-CC, i.e., temporary protecting DSBs and single-strand regions from repair machinery. The chromosomal bridges in arrest breakthrough cells suggest that RAD21L mei-CC generates physical linkage between the chromatids, which persists because this complex is resistant to the somatic prophase cohesin-removal pathway (74, 108–110) in the absence (our RNA-seq metadata) of the meiosis-specific NEK-PP1gamma cascade component (111).

The ability of RAD21L cohesin to coexist with condensin on chromosomes further indicates that the former remodels chromosomes in a meiosis-like fashion. Moreover, upon aberrant activation, RAD21L mei-CC might interfere with prophase functions of condensin such as chromosome and centromere individualization (112, 113), exacerbating potential chromosome damage. It was also evident that interphase chromosome condensation was coordinated with the RAD21L filaments' assembly and extension, while the filaments were much less pronounced over rDNA and telomeres, again similarly to meiotic prophase (45, 114, 115). The emergence of nuclei with paired chromosomes (Fig. 5) was an additional argument for the hypothesis that RAD21L filaments are functional analogs of mei-CC axes assembled in leptotene and are capable of maintaining the adhesion between the homologous chromosomes, without involvement of other meiosis-specific factors.

Proliferation Arrest and Chromosome Instability Are Probable Selection Factors against Mei-Cohesin Activation in Soma. We fully understand that our experiments on ectopic expression of mei-CC in cells in culture are only a model of real multistep processes that might undergo in soma of living organism. The experimental results nevertheless offer a set of revealing clues on the nature and putative dangers of unscheduled activation of particular CT genes. Particularly, based on the present study, we could infer that REC8 mei-CC presence in mitotically proliferating cells, while likely undesirable, can be overcome without cell-cycle arrest and/or damage, thus explaining why the expression of REC8 is permissible in various tumors (Fig. 1, *SI Appendix*, Fig. S10*C*). The diminished AuroraB localization to unattached kinetochores upon the ectopic REC8 mei-CC expression indicates a possible interference with kinetochore signaling (116). This defect is likely due to REC8 mei-CC binding to centromeres accompanied by the absence of key meiotic regulatory factors of this complex (54, 117).

In contrast, for the RAD21L mei-CC, we could hypothesize that there could be a dual mechanism behind its underrepresentation in tumors. First, RAD21L might be able to transiently compete with RAD21, affecting proliferation rate (Fig. 2*B*), which could be a negative factor for a clonal selection in tumors (*SI Appendix*, Fig. S10*D*). Second, the coexpression of RAD21L with SMC1B and STAG3, which are coregulated and are frequently coactivated in tumors (Fig. 1 *B–E*, *SI Appendix*, Fig. S10*C*), would disrupt proliferation by inducing cell-cycle arrest and by impairing the accuracy of chromosome segregation in cells that still passed through mitosis (*SI Appendix*, Fig. S10*D*). This hypothetical course of events would conceivably result in a population of arrested cells that nevertheless constantly produce chromosome instability. Furthermore, at a subsequent phase, if such a population finds a way

to epigenetically shut down the expression of RAD21L, it might reenter the proliferation but with a genetic load of chromosomal mutations (*SI Appendix*, Fig. S10*D*). As a result of either of two scenarios, RAD21L expression would be disfavored in actively proliferating tumors. Such a down-regulation of toxic chromatin components in developed and/or high-grade tumors is not unprecedented (10, 118). However, it does not exclude a possibility that RAD21L could be transiently activated in early oncogenic events (*SI Appendix*, Fig. S10*D*).

Methods

Cell Cultures and Ectopic Gene Expression Transgenes. K562 (ATCC CCL-243), DLD-1 (ATCC CCL-221), hTERT RPE (RPE-1, ATCC CRL-4000), and HTB-131 (ATCC HTB-131) cell lines were cultivated in IMDM (HyClone) with 10% or 20% Tet-grade fetal bovine serum (FBS). HEK293(ATCC CRL-1573) and HEK293T/17 (ATCC CRL-11268) cell lines were grown in Dulbecco's modified Eagle's medium (HyClone) with 10% FBS. Plasmid transfections were performed according to manufacturer suggestions using Roche transfection reagent X-tremeGENE9DNA. For packaging of lentivirus vectors, HEK293T/17 cells were cotransfected with packaging plasmids psPAX2 and Pmd2.G and custom constructs (*SI Appendix*, Table S1). Lentivirus particles were collected 72 h later. Details on gene expression, gene targeting (119), and stable cell lines are in *SI Appendix*.

RNA Interference (RNAi). The RNAi knockdown experiments were performed with three cell lines: DLD-1^{RAD21mNeonGreen}, DLD-1$^{SMC1B\text{-}STAG3\text{-}RAD21L}$, and DLD-1$^{SMC1B\text{-}STAG3\text{-}REC8}$ constructed as described above. The small interfering RNA (siRNA) (Guangzhou RiboBio Co.) against *WAPL*, PDS5A, and *PDS5B* were as in ref. 73; 100 nM, or 5 μL per six-well plate, of each siRNA was used for the transfection using oligomer–Lipofectamine 3000 complexes. Cells were incubated at 37 °C in a CO_2 incubator for 72 h before harvesting for analysis.

Chromatin fractionation was as described in ref. 120. Details on the modifications are in *SI Appendix*.

Antibodies (Ab). To generate custom Ab against human mei-CC subunits (RAD21L, REC8, STAG3, and SMC1B) only the nonoverlapping regions from paralogous proteins were selected and combined into artificial fusions by DNA synthesis (GenScript). The synthesized DNA was cloned into two vectors for heterologous *Escherichia coli* expression: pET15b (Novagen) and pGEX-6P-1 (GEHealthcare Lifesciences). The pET15b constructs were used to produce antigens for immunizations. Ab were purified using the corresponding pGEX-6P-1 recombinant constructs, as described in ref. 121. Details of Ab handling and staining as well as for commercial Ab are in *SI Appendix*. Anti-BORIS monoclonal Abs were generated in our previous work (10).

Epigenomic Methods. All primate work has been conducted at dedicated facilities in accordance with the ethical rules according to international guidelines (122, 123) and has been approved by the institutional review board. The cynomolgus monkey testis material was collected from six 7- to 9-y-old male monkeys (Wincon TheraCells Biotech), which were killed for an unrelated pharmacological study. The animal protocol was amended to include testis removal and processing onsite. The protocol was compliant with Good Laboratory Practices and the guidelines of World Health Organization Quality Practices in Basic Biomedical Research, and with all relevant government regulations. Pilot ChIP experiments were conducted with *Macaca rhesus* testis material obtained from two animals that died in fights at Guangdong Blue Island (Landao) Biotechnology Co., Ltd, Guangzhou, within 6 h postmortem. The material for testis fractionation by FACS was obtained from control animals in unrelated studies, from Huazhen Animal Farm and Landao Biotechnology Co. (both Guangzhou). Additional details are in *SI Appendix*.

For human cells ChIP-on-ChEP-seq, all experiments were conducted using cells cultured in vitro. Cell lines included immortalized human somatic cells (RPE-1 and its transgenic variants) or cancer cells (K562, DLD-1, HTB-131, and their transgenic variants). To analyze chromatin protein binding we adapted a published strategy named ChEP, or Chromatin Enriched for Proteomics (124, 125), enabling the extraction of pure fixed chromatin under chaotropic conditions. Fixed testis germ cells samples were thawed on ice and remeshed in cold phosphate-buffered saline (PBS) through a 40-μm cell strainer. Germ cells were washed twice in cold PBS to remove smaller debris. The purity of germ cells population was confirmed by microscopy with staining for nuclear DNA and DDX4 IF. Additional preparation details are in *SI Appendix*.

ATAC-seq was carried out as described with minor modifications (62). We performed size selection to eliminate the bulk of primer–dimer artifacts after libraries amplifications as described (126). Specific technique details are in *SI Appendix*.

FACS. Adherent cells were treated with trypsin for 3 min and harvested, washed three times with DPBS, and pelleted. After resuspending in 0.3 mL of DPBS cells were fixed with 0.75 mL of ice-cold pure ethanol, added drop by drop while vortexing, followed by 4 °C incubation for up to 1 wk. For staining, 200 to 400 μL of PI/RNase Staining Buffer Solution (BD Pharmingen) was added to cells with gentle resuspending with pipette tip and incubated at 37 °C for 15 min. The suspension of cells was analyzed by flow cytometry using BD LSR Fortessa SORP.

For sorting monkey testis cells, a protocol was modified from ref. 127. Briefly, on the day of sorting, fixed germ cells frozen in 20% glycerol, DBPS, were thawed on ice, counted and incubated with 5 μg/10^6 germ cells of Hoechst 33342 (H3570; Life Technologies) for 30 min. Typically, 5 to 6 × 10^7 germ cells were used per sorting. Germ cells were passed through a 40-μm cell strainer to obtain mostly a single cell suspension. MoFlo Astrios EQ cell sorter (Beckman Coulter) was set with following parameters: 100-μm nozzle size, pressure 25 psi, 40,000-Hz frequency, 30 to 50 approximate drop delay 40, polypropylene collection tubes (352063; Falcon), purify abort mode, 7,000 to 8,000 EPS separation speed. Flow cytometry detectors were set for Hoechst Blue (UV355-460/50) and Hoechst Red (UV355-670/30). After sorting, an aliquot from each fraction was set aside for IF and cell count, and the rest was centrifuged at 1,500 rpm at 4C degree for 10 min. After supernatant removal samples were flash-frozen directly in liquid nitrogen.

For BrdU FACS, the APC BrdU Flow Kit (552598; BD Pharmingen) was used. Staining and procedures were done according to the manufacturer's recommendation, and cell suspension was analyzed with BD LSR Fortessa SORP Flow Cytometer, with high voltage setting. A minimum of 20 × 10^3 cells were recorded for all FACS experiments.

Bioinformatic Analysis. As a routine approach, the ChIP-on-ChEP-seq data (delivered as paired reads) from crab-eating macaque were first cleaned by trimming of adapters and removing low-quality reads using fastp (128). Then, reads were aligned to whole assembled genome, i.e., Macfas5, NCBI Assembly ID 704988, including all fragments and scaffolds, with Bowtie 2 (129). Bowtie 2 parameters were –bowtie2-sensisitvity-level very_sensitive k 5. The initial peak calling was done using MACS2.2 (130, 131) and was limited to 21 *M. fascicularis* female chromosomes. Peaks were selectively validated by qPCR. Some additional peak filtering was done for most analyses. First, the summits of high-confidence peaks were intersected with RepeatMasker (RM) and Tandem Repeat Finder (TRF) datasets and the peaks with summits falling into genomic repeats were excluded. Second, peaks from the two biological replicates were intersected with each other with bedtools (132), with –d 10 parameter or with Genome Integrator (UCSC utilities), to generate a set of conserved peaks. Finally, a "superset" was generated by eliminating noisy and weakly enriched intervals revealed as a result of sequence tag density clustering using DeepTools (133) or Seqminer (134).

For epigenomic enrichment annotation relative to gene features, peaks that were specific to each factor were analyzed using R (v4.0.3) with the ChIPseeker package (v 1.26.0, https://www.bioconductor.org/) and the annotatePeak function, using tssRegion = c(−3000,3000) option and a TxDb built from Ensembl *M. fascicularis* database of transcripts (asia.ensembl.org). For ATAC-seq, peaks were identified by Genrich v.0.6.1 (https://github.com/jsh58/Genrich), in ATAC-seq mode. The resulting tag density files were used for differential analyses. The ATAC-seq peak annotations were done with GeneHancer (135).

For GO analysis/clustering and pathway mapping, ClusterProfiler (https://guangchuangyu.github.io/software/clusterProfiler) and KEGG portal (https://genome.jgi.doe.gov/portal/) were used. To associate peaks with genes and control elements, Homer (136) and GeneHancer (135) were used, dependent on the application. Gene name conversion was done using the NCBI Gene geneinfo file, ClusterProfiler, or AnnotationDbi::mapIds tool (bioconductor.org/packages/release/bioc/html/AnnotationDbi.html). Enriched GO terms were determined for each group using enrichGO from clusterProfiler package v 3.12.0 in R v 3.6.0, with results combined using the compareCluster function and plotted using the dotplot function.

DSB maps of human meiosis were from ref. 137. Human BORIS and CTCF ChIP-seq data were derived from our prior publication (10), except they were realigned to hg38.

RNA-Seq Analysis. RNA-seq experiments were designed, performed, and analyzed using standard approaches, as described in *SI Appendix*.

Proteome Analysis by Mass Spectrometry. The mass spectrometry analysis by iTRAQ (Multiplexed Isobaric Tagging Technology for Relative Quantitation) was conducted at the BGI (Shenzhen) mass spectrometry laboratory. The full iTRAQ protocol used can be found at https://sciex.com/content/dam/SCIEX/pdf/brochures/mass-spectrometry-4375249C.pdf and the list of iTRAQ reagents at https://www.sciex.com/products/standards-and-reagents/itraq-reagents. IQuant software (138) was used to quantify labeled peptides with isobaric tags. Specific details on experimental design and sample preparation are described in *SI Appendix*.

Data, Materials, and Software Availability. High-throughput sequencing data and corresponding metadata were deposited to NCBI GEO with the following accession numbers: GSE118006 (139), GSE142746 (140), GSE142247 (141), and GSE201683 (142). Mass-spectrometry data were deposited at the ProteomeXchange website, ID = PXD024713 (143). All other study data are included in the article and/or supporting information.

ACKNOWLEDGMENTS. This work was supported by the MOST National Key R&D Program of China project number 2018YFA0106903 to A.V.S. and M.E. Additional funding to A.S. was from the Government of Guangdong province. Support to A.A. and M.D. was by the Intramural Research Program of the Eunice Kennedy Shriver National Institute of Child Health and Human Development, NIH. V.L. and E.M.P. were supported by the Intramural Research Program of the National Institute of Allergy and Infectious Diseases, NIH. We thank former laboratory members J. Y. Zhang, J. J. Li, and C. C. Meng for the initial purification and characterization of custom antibodies; V. Ogryzko for the RPE-1 clone; M. Tortotella (GIBH), Liu Wei (Huazhen Farm), and Xiangyu Guo (Landao Co.) for macaque tissues; D. Loukinov and M. Lichten for productive discussion.

Author affiliations: [a]Molecular Epigenetics Laboratory, Guangzhou Institutes of Biomedicine and Health, Guangzhou 510530, China; [b]South China Institute for Stem Cell Biology and Regenerative Medicine, Guangzhou Institutes of Biomedicine and Health, Guangzhou 510530, China; [c]National Institute of Child Health and Human Development, Section on Cell Cycle Regulation, NIH, Bethesda, MD 20892; and [d]Laboratory of Immunogenetics, National Institute of Allergy and Infectious Diseases, NIH, Bethesda, MD 20852

1. M. J. Scanlan, A. J. Simpson, L. J. Old, The cancer/testis genes: Review, standardization, and commentary. *Cancer Immun.* **4**, 1 (2004).
2. K. E. Maxfield *et al.*, Comprehensive functional characterization of cancer-testis antigens defines obligate participation in multiple hallmarks of cancer. *Nat. Commun.* **6**, 8840 (2015).
3. C. Wang *et al.*, Systematic identification of genes with a cancer-testis expression pattern in 19 cancer types. *Nat. Commun.* **7**, 10499 (2016).
4. N. Qin *et al.*, Systematic identification of long non-coding RNAs with cancer-testis expression patterns in 14 cancer types. *Oncotarget* **8**, 94769–94779 (2017).
5. F. Chen *et al.*, Pan-cancer molecular classes transcending tumor lineage across 32 cancer types, multiple data platforms, and over 10,000 cases. *Clin. Cancer Res.* **24**, 2182–2193 (2018).
6. Y. T. Chen *et al.*, A testicular antigen aberrantly expressed in human cancers detected by autologous antibody screening. *Proc. Natl. Acad. Sci. U.S.A.* **94**, 1914–1918 (1997).
7. Z. A. Gibbs, A. W. Whitehurst, Emerging contributions of cancer/testis antigens to neoplastic behaviors. *Trends Cancer* **4**, 701–712 (2018).
8. M. T. Epping *et al.*, The human tumor antigen PRAME is a dominant repressor of retinoic acid receptor signaling. *Cell* **122**, 835–847 (2005).
9. N. Hosoya *et al.*, Synaptonemal complex protein SYCP3 impairs mitotic recombination by interfering with BRCA2. *EMBO Rep.* **13**, 44–51 (2011).
10. E. M. Pugacheva *et al.*, Comparative analyses of CTCF and BORIS occupancies uncover two distinct classes of CTCF binding genomic regions. *Genome Biol.* **16**, 161 (2015).
11. A. K. Michael *et al.*, Cancer/testis antigen PASD1 silences the circadian clock. *Mol. Cell* **58**, 743–754 (2015).
12. F. Rossi *et al.*, An *in vivo* genetic screen in *Drosophila* identifies the orthologue of human cancer/testis gene *SPO11* among a network of targets to inhibit *lethal(3)malignant brain tumour* growth. *Open Biol.* **7**, 170156 (2017).
13. Y. Hosono *et al.*, Oncogenic role of THOR, a conserved cancer/testis long non-coding RNA. *Cell* **171**, 1559–1572 e1520 (2017).
14. D. N. Debruyne *et al.*, BORIS promotes chromatin regulatory interactions in treatment-resistant cancer cells. *Nature* **572**, 676–680 (2019).
15. P. A. Jones, H. Ohtani, A. Chakravarthy, D. D. De Carvalho, Epigenetic therapy in immune-oncology. *Nat. Rev. Cancer* **19**, 151–161 (2019).
16. M. Liskovykh *et al.*, A novel assay to screen siRNA libraries identifies protein kinases required for chromosome transmission. *Genome Res.* **29**, 1719–1732 (2019).
17. I. Martincorena *et al.*, Universal patterns of selection in cancer and somatic tissues. *Cell* **171**, 1029–1041.e21 (2017).
18. E. Porta-Pardo *et al.*, Comparison of algorithms for the detection of cancer drivers at subgene resolution. *Nat. Methods* **14**, 782–788 (2017).
19. N. Auslander, Y. I. Wolf, E. V. Koonin, In silico learning of tumor evolution through mutational time series. *Proc. Natl. Acad. Sci. U.S.A.* **116**, 9501–9510 (2019).
20. A. Strunnikov, Cohesin complexes with a potential to link mammalian meiosis to cancer. *Cell Regen. (Lond.)* **2**, 4 (2013).
21. A. Y. Nielsen, M. F. Gjerstorff, Ectopic expression of testis germ cell proteins in cancer and its potential role in genomic instability. *Int. J. Mol. Sci.* **17**, E890 (2016).
22. A. Jay, D. Reitz, S. H. Namekawa, W. D. Heyer, Cancer testis antigens and genomic instability: More than immunology. *DNA Repair (Amst.)* **108**, 103214 (2021).
23. P. J. Stephens *et al.*, Massive genomic rearrangement acquired in a single catastrophic event during cancer development. *Cell* **144**, 27–40 (2011).
24. M. Liu *et al.*, Meta-analysis of microarray datasets identify several chromosome segregation-related cancer/testis genes potentially contributing to anaplastic thyroid carcinoma. *PeerJ* **6**, e5822 (2018).
25. M. Ratnaparkhe *et al.*, Defective DNA damage repair leads to frequent catastrophic genomic events in murine and human tumors. *Nat. Commun.* **9**, 4760 (2018).
26. P. Ly *et al.*, Chromosome segregation errors generate a diverse spectrum of simple and complex genomic rearrangements. *Nat. Genet.* **51**, 705–715 (2019).
27. J. Maciejowski *et al.*, APOBEC3-dependent kataegis and TREX1-driven chromothripsis during telomere crisis. *Nat. Genet.* **52**, 884–890 (2020).
28. O. Shoshani *et al.*, Chromothripsis drives the evolution of gene amplification in cancer. *Nature* **591**, 137–141 (2021).
29. N. T. Umbreit *et al.*, Mechanisms generating cancer genome complexity from a single cell division error. *Science* **368**, eaba0712 (2020).
30. O. Wood *et al.*; SPARC Consortium, Gene expression analysis of TIL rich HPV-driven head and neck tumors reveals a distinct B-cell signature when compared to HPV independent tumors. *Oncotarget* **7**, 56781–56797 (2016).
31. I. V. Litvinov *et al.*, Ectopic expression of cancer-testis antigens in cutaneous T-cell lymphoma patients. *Clin. Cancer Res.* **20**, 3799–3808 (2014).
32. K. Nasmyth, A meiotic mystery: How sister kinetochores avoid being pulled in opposite directions during the first division. *BioEssays* **37**, 657–665 (2015).
33. D. Liu, X. Shen, G. Zhu, M. Xing, REC8 is a novel tumor suppressor gene epigenetically robustly targeted by the PI3K pathway in thyroid cancer. *Oncotarget* **6**, 39211–39224 (2015).
34. M. Rong, S. Miyauchi, J. Lee, Ectopic expression of meiotic cohesin RAD21L promotes adjacency of homologous chromosomes in somatic cells. *J. Reprod. Dev.* **63**, 227–234 (2017).
35. H. D. Folco *et al.*, Untimely expression of gametogenic genes in vegetative cells causes uniparental disomy. *Nature* **543**, 126–130 (2017).
36. D. Q. Ding *et al.*, Meiotic cohesin-based chromosome structure is essential for homologous chromosome pairing in Schizosaccharomyces pombe. *Chromosoma* **125**, 205–214 (2016).
37. R. Jessberger, Cohesin complexes get more complex: The novel kleisin RAD21L. *Cell Cycle* **10**, 2053–2054 (2011).
38. J. Lee, T. Hirano, RAD21L, a novel cohesin subunit implicated in linking homologous chromosomes in mammalian meiosis. *J. Cell Biol.* **192**, 263–276 (2011).
39. K. Ishiguro, J. Kim, S. Fujiyama-Nakamura, S. Kato, Y. Watanabe, A new meiosis-specific cohesin complex implicated in the cohesin code for homologous pairing. *EMBO Rep.* **12**, 267–275 (2011).
40. Y. Herrán *et al.*, The cohesin subunit RAD21L functions in meiotic synapsis and exhibits sexual dimorphism in fertility. *EMBO J.* **30**, 3091–3105 (2011).
41. T. Fukuda *et al.*, STAG3-mediated stabilization of REC8 cohesin complexes promotes chromosome synapsis during meiosis. *EMBO J.* **33**, 1243–1255 (2014).
42. M. Rong, A. Matsuda, Y. Hiraoka, J. Lee, Meiotic cohesin subunits RAD21L and REC8 are positioned at distinct regions between lateral elements and transverse filaments in the synaptonemal complex of mouse spermatocytes. *J. Reprod. Dev.* **62**, 623–630 (2016).
43. A. Agostinho *et al.*, High density of REC8 constrains sister chromatid axes and prevents illegitimate synaptonemal complex formation. *EMBO Rep.* **17**, 901–913 (2016).
44. A. Ward, J. Hopkins, M. Mckay, S. Murray, P. W. Jordan, Genetic interactions between the meiosis-specific cohesin components, STAG3, REC8, and RAD21L. *G3 (Bethesda)* **6**, 1713–1724 (2016).
45. K. Ishiguro *et al.*, Meiosis-specific cohesin mediates homolog recognition in mouse spermatocytes. *Genes Dev.* **28**, 594–607 (2014).
46. U. Biswas, K. Hempel, E. Llano, A. Pendas, R. Jessberger, Distinct roles of meiosis-specific cohesin complexes in mammalian spermatogenesis. *PLoS Genet.* **12**, e1006389 (2016).
47. K. I. Ishiguro, The cohesin complex in mammalian meiosis. *Genes Cells* **24**, 6–30 (2019).
48. E. Llano *et al.*, Meiotic cohesin complexes are essential for the formation of the axial element in mice. *J. Cell Biol.* **197**, 877–885 (2012).
49. A. Kouznetsova, R. Benavente, A. Pastink, C. Höög, Meiosis in mice without a synaptonemal complex. *PLoS One* **6**, e28255 (2011).
50. L. A. Bannister, L. G. Reinholdt, R. J. Munroe, J. C. Schimenti, Positional cloning and characterization of mouse mei8, a disrupted allelle of the meiotic cohesin Rec8. *Genesis* **40**, 184–194 (2004).
51. E. Revenkova *et al.*, Cohesin SMC1 beta is required for meiotic chromosome dynamics, sister chromatid cohesion and DNA recombination. *Nat. Cell Biol.* **6**, 555–562 (2004).
52. J. A. Suja, J. L. Barbero, Cohesin complexes and sister chromatid cohesion in mammalian meiosis. *Genome Dyn.* **5**, 94–116 (2009).
53. E. D. Parvanov *et al.*, PRDM9 interactions with other proteins provide a link between recombination hotspots and the chromosomal axis in meiosis. *Mol. Biol. Cell* **28**, 488–499 (2017).
54. J. Hopkins *et al.*, Meiosis-specific cohesin component, Stag3 is essential for maintaining centromere chromatid cohesion, and required for DNA repair and synapsis between homologous chromosomes. *PLoS Genet.* **10**, e1004413 (2014).
55. K. Ishiguro, Y. Watanabe, The cohesin REC8 prevents illegitimate inter-sister synaptonemal complex assembly. *EMBO Rep.* **17**, 783–784 (2016).
56. K. Tachibana-Konwalski *et al.*, Rec8-containing cohesin maintains bivalents without turnover during the growing phase of mouse oocytes. *Genes Dev.* **24**, 2505–2516 (2010).

57. C. H. Shen *et al.*, Loss of cohesin complex components STAG2 or STAG3 confers resistance to BRAF inhibition in melanoma. *Nat. Med.* **22**, 1056–1061 (2016).
58. M. Sasaki *et al.*, The meiosis-specific cohesin component stromal antigen 3 promotes cell migration and chemotherapeutic resistance in colorectal cancer. *Cancer Lett.* **497**, 112–122 (2021).
59. P. Samaras *et al.*, ProteomicsDB: A multi-omics and multi-organism resource for life science research. *Nucleic Acids Res.* **48**, D1153–D1163 (2020).
60. J. H. Kim *et al.*, High cleavage efficiency of a 2A peptide derived from porcine teschovirus-1 in human cell lines, zebrafish and mice. *PLoS One* **6**, e18556 (2011).
61. M. D. Ryan, J. Drew, Foot-and-mouth disease virus 2A oligopeptide mediated cleavage of an artificial polyprotein. *EMBO J.* **13**, 928–933 (1994).
62. J. D. Buenrostro, B. Wu, H. Y. Chang, W. J. Greenleaf, ATAC-seq: A method for assaying chromatin accessibility genome-wide. *Curr. Protoc. Mol. Biol.* **109**, 21.29.1–21.29.9 (2015).
63. M. L. Kojima, D. G. de Rooij, D. C. Page, Amplification of a broad transcriptional program by a common factor triggers the meiotic cell cycle in mice. *eLife* **8**, e43738 (2019).
64. J. Guo *et al.*, The adult human testis transcriptional cell atlas. *Cell Res.* **28**, 1141–1157 (2018).
65. J. H. I. Haarhuis *et al.*, The cohesin release factor WAPL restricts chromatin loop extension. *Cell* **169**, 693–707.e14 (2017).
66. S. S. P. Rao *et al.*, Cohesin loss eliminates all loop domains. *Cell* **171**, 305–320.e24 (2017).
67. E. M. Pugacheva *et al.*, CTCF mediates chromatin looping via N-terminal domain-dependent cohesin retention. *Proc. Natl. Acad. Sci. U.S.A.* **117**, 2020–2031 (2020).
68. A. N. Shami *et al.*, Single-cell RNA sequencing of human, macaque, and mouse testes uncovers conserved and divergent features of mammalian spermatogenesis. *Dev. Cell* **54**, 529–547.e12 (2020).
69. X. Lau, P. Munusamy, M. J. Ng, M. Sangrithi, Single-cell RNA sequencing of the cynomolgus macaque testis reveals conserved transcriptional profiles during mammalian spermatogenesis. *Dev. Cell* **54**, 548–566.e7 (2020).
70. V. Gaysinskaya *et al.*, Transient reduction of DNA methylation at the onset of meiosis in male mice. *Epigenetics Chromatin* **11**, 15 (2018).
71. M. Uhlén *et al.*, Proteomics. Tissue-based map of the human proteome. *Science* **347**, 1260419 (2015).
72. S. Rivero-Hinojosa *et al.*, The combined action of CTCF and its testis-specific paralog BORIS is essential for spermatogenesis. *Nat. Commun.* **12**, 3846 (2021).
73. G. Wutz *et al.*, Topologically associating domains and chromatin loops depend on cohesin and are regulated by CTCF, WAPL, and PDS5 proteins. *EMBO J.* **36**, 3573–3599 (2017).
74. Y. Murayama, F. Uhlmann, DNA entry into and exit out of the cohesin ring by an interlocking gate mechanism. *Cell* **163**, 1628–1640 (2015).
75. N. Walther *et al.*, A quantitative map of human Condensins provides new insights into mitotic chromosome architecture. *J. Cell Biol.* **217**, 2309–2328 (2018).
76. T. Ono, D. Yamashita, T. Hirano, Condensin II initiates sister chromatid resolution during S phase. *J. Cell Biol.* **200**, 429–441 (2013).
77. Z. Y. Lin *et al.*, Gene expression ontogeny of spermatogenesis in the marmoset uncovers primate characteristics during testicular development. *Dev. Biol.* **400**, 43–58 (2015).
78. G. Margolin, P. P. Khil, J. Kim, M. A. Bellani, R. D. Camerini-Otero, Integrated transcriptome analysis of mouse spermatogenesis. *BMC Genomics* **15**, 39 (2014).
79. S. S. Hammoud *et al.*, Chromatin and transcription transitions of mammalian adult germline stem cells and spermatogenesis. *Cell Stem Cell* **15**, 239–253 (2014).
80. C. Vara *et al.*, Three-dimensional genomic structure and cohesin occupancy correlate with transcriptional activity during spermatogenesis. *Cell Rep.* **28**, 352–367.e9 (2019).
81. B. P. Hermann *et al.*, The mammalian spermatogenesis single-cell transcriptome, from spermatogonial stem cells to spermatids. *Cell Rep.* **25**, 1650–1667 e1658 (2018).
82. K. S. Wendt *et al.*, Cohesin mediates transcriptional insulation by CCCTC-binding factor. *Nature* **451**, 796–801 (2008).
83. S. S. Rao *et al.*, A 3D map of the human genome at kilobase resolution reveals principles of chromatin looping. *Cell* **159**, 1665–1680 (2014).
84. A. L. Sanborn *et al.*, Chromatin extrusion explains key features of loop and domain formation in wild-type and engineered genomes. *Proc. Natl. Acad. Sci. U.S.A.* **112**, E6456–E6465 (2015).
85. L. Vian *et al.*, The energetics and physiological impact of cohesin extrusion. *Cell* **175**, 292–294 (2018).
86. J. Nuebler, G. Fudenberg, M. Imakaev, N. Abdennur, L. A. Mirny, Chromatin organization by an interplay of loop extrusion and compartmental segregation. *Proc. Natl. Acad. Sci. U.S.A.* **115**, E6697–E6706 (2018).
87. Z. Deng *et al.*, A role for CTCF and cohesin in subtelomere chromatin organization, TERRA transcription, and telomere end protection. *EMBO J.* **31**, 4165–4178 (2012).
88. G. Fudenberg *et al.*, Formation of chromosomal domains by loop extrusion. *Cell Rep.* **15**, 2038–2049 (2016).
89. L. Ren *et al.*, CTCF and cohesin cooperatively mediate the cell-type specific interchromatin interaction between Bcl11b and Arhgap6 loci. *Mol. Cell. Biochem.* (2011).
90. A. J. Feeney, J. Verma-Gaur, CTCF-cohesin complex: Architect of chromatin structure regulates V(D)J rearrangement. *Cell Res.* **22**, 280–282 (2012).
91. Y. Guo *et al.*, CTCF/cohesin-mediated DNA looping is required for protocadherin α promoter choice. *Proc. Natl. Acad. Sci. U.S.A.* **109**, 21081–21086 (2012).
92. T. Nozaki *et al.*, Dynamic organization of chromatin domains revealed by super-resolution live-cell imaging. *Mol. Cell* **67**, 282–293.e7 (2017).
93. J. Holzmann *et al.*, Absolute quantification of cohesin, CTCF and their regulators in human cells. *eLife* **8**, e46269 (2019).
94. G. A. Busslinger *et al.*, Cohesin is positioned in mammalian genomes by transcription, CTCF and Wapl. *Nature* **544**, 503–507 (2017).
95. E. P. Nora *et al.*, Targeted degradation of CTCF decouples local insulation of chromosome domains from genomic compartmentalization. *Cell* **169**, 930–944.e22 (2017).
96. S. S. Teves *et al.*, A dynamic mode of mitotic bookmarking by transcription factors. *eLife* **5**, e46314 (2016).
97. A. Steube, T. Schenk, A. Tretyakov, H. P. Saluz, High-intensity UV laser ChIP-seq for the study of protein-DNA interactions in living cells. *Nat. Commun.* **8**, 1303 (2017).
98. M. P. Meers, T. D. Bryson, J. G. Henikoff, S. Henikoff, Improved CUT&RUN chromatin profiling tools. *eLife* **8**, e46314 (2019).
99. T. Sakata, K. Shirahige, T. Sutani, ChIP-seq analysis of condensin complex in cultured mammalian cells. *Methods Mol. Biol.* **1515**, 257–271 (2017).
100. M. E. Oomen, A. S. Hansen, Y. Liu, X. Darzacq, J. Dekker, CTCF sites display cell cycle-dependent dynamics in factor binding and nucleosome positioning. *Genome Res.* **29**, 236–249 (2019).
101. S. Renaud *et al.*, Expression of the CTCF-paralogous cancer-testis gene, brother of the regulator of imprinted sites (BORIS), is regulated by three alternative promoters modulated by CpG methylation and by CTCF and p53 transcription factors. *Nucleic Acids Res.* **35**, 7372–7388 (2007).
102. T. Suzuki *et al.*, Expression of a testis-specific form of Gal3st1 (CST), a gene essential for spermatogenesis, is regulated by the CTCF paralogous gene BORIS. *Mol. Cell. Biol.* **30**, 2473–2484 (2010).
103. F. Sleutels *et al.*, The male germ cell gene regulator CTCFL is functionally different from CTCF and binds CTCF-like consensus sites in a nucleosome composition-dependent manner. *Epigenetics Chromatin* **5**, 8 (2012).
104. K. Hara *et al.*, Structure of cohesin subcomplex pinpoints direct shugoshin-Wapl antagonism in centromeric cohesion. *Nat. Struct. Mol. Biol.* **21**, 864–870 (2014).
105. F. Yang *et al.*, Mouse SYCP2 is required for synaptonemal complex assembly and chromosomal synapsis during male meiosis. *J. Cell Biol.* **173**, 497–507 (2006).
106. J. Pelttari *et al.*, A meiotic chromosomal core consisting of cohesin complex proteins recruits DNA recombination proteins and promotes synapsis in the absence of an axial element in mammalian meiotic cells. *Mol. Cell. Biol.* **21**, 5667–5677 (2001).
107. A. Kouznetsova, I. Novak, R. Jessberger, C. Höög, SYCP2 and SYCP3 are required for cohesin core integrity at diplotene but not for centromere cohesion at the first meiotic division. *J. Cell Sci.* **118**, 2271–2278 (2005).
108. A. Tedeschi *et al.*, Wapl is an essential regulator of chromatin structure and chromosome segregation. *Nature* **501**, 564–568 (2013).
109. J. H. Haarhuis *et al.*, WAPL-mediated removal of cohesin protects against segregation errors and aneuploidy. *Curr. Biol.* **23**, 2071–2077 (2013).
110. F. Beckouët *et al.*, Releasing activity disengages cohesin's Smc3/Scc1 interface in a process blocked by acetylation. *Mol. Cell* **61**, 563–574 (2016).
111. M. A. Brieño-Enríquez *et al.*, Cohesin removal along the chromosome arms during the first meiotic division depends on a NEK1-PP1γ-WAPL axis in the mouse. *Cell Rep.* **17**, 977–986 (2016).
112. K. Nishide, T. Hirano, Overlapping and non-overlapping functions of condensins I and II in neural stem cell divisions. *PLoS Genet.* **10**, e1004847 (2014).
113. M. Houlard *et al.*, Condensin confers the longitudinal rigidity of chromosomes. *Nat. Cell Biol.* **17**, 771–781 (2015).
114. M. Tsutsumi *et al.*, Characterization of a novel mouse gene encoding an SYCP3-like protein that relocalizes from the XY body to the nucleolus during prophase of male meiosis I. *Biol. Reprod.* **85**, 165–171 (2011).
115. J. Long *et al.*, Telomeric TERB1-TRF1 interaction is crucial for male meiosis. *Nat. Struct. Mol. Biol.* **24**, 1073–1080 (2017).
116. M. A. Lampson, I. M. Cheeseman, Sensing centromere tension: Aurora B and the regulation of kinetochore function. *Trends Cell Biol.* **21**, 133–140 (2011).
117. S. Burkhardt *et al.*, Chromosome cohesion established by Rec8-cohesin in fetal oocytes is maintained without detectable turnover in oocytes arrested for months in mice. *Curr. Biol.* **26**, 678–685 (2016).
118. A. Taber *et al.*, STAG2 as a prognostic biomarker in low-grade non-muscle invasive bladder cancer. *Urol. Oncol.* **39**, 438 e431–438 e439 (2021).
119. L. Cong *et al.*, Multiplex genome engineering using CRISPR/Cas systems. *Science* **339**, 819–823 (2013).
120. J. Wysocka, P. T. Reilly, W. Herr, Loss of HCF-1-chromatin association precedes temperature-induced growth arrest of tsBN67 cells. *Mol. Cell. Biol.* **21**, 3820–3829 (2001).
121. E. A. Greenfield, *Antibodies: A Laboratory Manual* (Cold Spring Harbor Laboratory, Cold Spring Harbor, NY, ed. 2, 2014).
122. D. J. Weatherall, *The Use of Non-Human Primates in Research* (Academy of Medical Sciences, 2006).
123. E. W. Lankau, P. V. Turner, R. J. Mullan, G. G. Galland, Use of nonhuman primates in research in North America. *J. Am. Assoc. Lab. Anim. Sci.* **53**, 278–282 (2014).
124. G. Kustatscher, K. L. Wills, C. Furlan, J. Rappsilber, Chromatin enrichment for proteomics. *Nat. Protoc.* **9**, 2090–2099 (2014).
125. T. Kohwi-Shigematsu *et al.*, SATB1-mediated functional packaging of chromatin into loops. *Methods* **58**, 243–254 (2012).
126. H. S. Kaya-Okur, D. H. Janssens, J. G. Henikoff, K. Ahmad, S. Henikoff, Efficient low-cost chromatin profiling with CUT&Tag. *Nat. Protoc.* **15**, 3264–3283 (2020).
127. V. Gaysinskaya, I. Y. Soh, G. W. van der Heijden, A. Bortvin, Optimized flow cytometry isolation of murine spermatocytes. *Cytometry A* **85**, 556–565 (2014).
128. S. Chen, Y. Zhou, Y. Chen, J. Gu, fastp: An ultra-fast all-in-one FASTQ preprocessor. *Bioinformatics* **34**, i884–i890 (2018).
129. B. Langmead, C. Trapnell, M. Pop, S. L. Salzberg, Ultrafast and memory-efficient alignment of short DNA sequences to the human genome. *Genome Biol.* **10**, R25 (2009).
130. Y. Zhang *et al.*, Model-based analysis of ChIP-Seq (MACS). *Genome Biol.* **9**, R137 (2008).
131. T. Liu, Use model-based analysis of ChIP-Seq (MACS) to analyze short reads generated by sequencing protein-DNA interactions in embryonic stem cells. *Methods Mol. Biol.* **1150**, 81–95 (2014).
132. A. R. Quinlan, BEDTools: The Swiss-army tool for genome feature analysis. *Curr. Protoc. Bioinformatics* **47**, 11.12.1–34 (2014).
133. F. Ramírez *et al.*, deepTools2: A next generation web server for deep-sequencing data analysis. *Nucleic Acids Res.* **44**, W160–W165 (2016).
134. T. Ye *et al.*, seqMINER: An integrated ChIP-seq data interpretation platform. *Nucleic Acids Res.* **39**, e35 (2011).
135. S. Fishilevich *et al.*, GeneHancer: Genome-wide integration of enhancers and target genes in GeneCards. *Database* **2017**, bax028 (2017).
136. S. Heinz *et al.*, Simple combinations of lineage-determining transcription factors prime cis-regulatory elements required for macrophage and B cell identities. *Mol. Cell* **38**, 576–589 (2010).
137. F. Pratto *et al.*, DNA recombination. Recombination initiation maps of individual human genomes. *Science* **346**, 1256442 (2014).
138. B. Wen *et al.*, IQuant: An automated pipeline for quantitative proteomics based upon isobaric tags. *Proteomics* **14**, 2280–2285 (2014).
139. A. Boukaba *et al.*, Ectopic expression of meiotic cohesin generates chromosome instability in cancer cell line. NCBI: GEO. https://www.ncbi.nlm.nih.gov/geo/query/acc.cgi?acc=GSE118006. Deposited 1 August 2018.
140. A. Boukaba *et al.*, Ectopic expression of meiotic cohesin generates chromosome instability in cancer cell line. NCBI: GEO. https://www.ncbi.nlm.nih.gov/geo/query/acc.cgi?acc=GSE142746. Deposited 30 December 2019.
141. A. Boukaba *et al.*, Ectopic expression of meiotic cohesin generates chromosome instability in cancer cell line. NCBI: GEO. https://www.ncbi.nlm.nih.gov/geo/query/acc.cgi?acc=GSE142247. Deposited 18 December 2019.
142. A. Boukaba *et al.*, Ectopic expression of meiotic cohesin generates chromosome instability in cancer cell line. NCBI: GEO. https://www.ncbi.nlm.nih.gov/geo/query/acc.cgi?acc=GSE201683. Deposited 27 April 2022.
143. A. Boukaba *et al.*, Ectopic expression of meiotic cohesin generates chromosome instability in cancer cell line. ProteomeXchange. http://proteomecentral.proteomexchange.org/cgi/GetDataset?ID=PXD024713. Deposited 12 March 2021.